

# 1 **Impact of HO<sub>2</sub>/RO<sub>2</sub> ratio on highly oxygenated $\alpha$ -pinene** 2 **photooxidation products and secondary organic aerosol formation** 3 **potential**

4 Yarê Baker<sup>1</sup>, Sungah Kang<sup>1</sup>, Hui Wang<sup>1</sup>, Rongrong Wu<sup>1</sup>, Jian Xu<sup>1</sup>, Annika Zanders<sup>1</sup>, Quanfu He<sup>1</sup>,  
5 Thorsten Hohaus<sup>1</sup>, Till Ziehm<sup>1</sup>, Veronica Geretti<sup>2</sup>, Thomas J. Bannan<sup>3</sup>, Simon P. O'Meara<sup>3,4</sup>, Aristeidis  
6 Voliotis<sup>3</sup>, Mattias Hallquist<sup>2</sup>, Gordon McFiggans<sup>3</sup>, Sören R. Zorn<sup>1</sup>, Andreas Wahner<sup>1</sup>, and Thomas F.  
7 Mentel<sup>1</sup>

8 <sup>1</sup>Institute for Energy and Climate Research, IEK-8, Forschungszentrum Jülich, 52425 Jülich, Germany

9 <sup>2</sup>Atmospheric Science, Dept. of Chemistry, University of Gothenburg, Gothenburg, 412 96, Sweden

10 <sup>3</sup>Department for Earth and Environmental Sciences, University of Manchester, Manchester, M13 9PL, UK

11 <sup>4</sup>National Centre for Atmospheric Science, University of Manchester, Manchester, M13 9PL, UK

12

13 *Correspondence to:* Thomas F. Mentel (t.mentel@fz-juelich.de)

14 **Abstract.** Highly oxygenated molecules (HOMs) from the atmospheric oxidation of biogenic volatile organic compounds  
15 are important contributors to secondary organic aerosol (SOA). Organic peroxy radicals (RO<sub>2</sub>) and hydroperoxy radicals  
16 (HO<sub>2</sub>) are key species influencing the HOM product distribution. In laboratory studies experimental requirements often  
17 result in overemphasis of RO<sub>2</sub> cross-reactions compared to reactions of RO<sub>2</sub> with HO<sub>2</sub>. We analyzed the photochemical  
18 formation of HOMs from  $\alpha$ -pinene and their potential to contribute to SOA formation under high ( $\approx 1/1$ ) and low ( $\approx 1/100$ )  
19 HO<sub>2</sub>/RO<sub>2</sub> conditions. As HO<sub>2</sub>/RO<sub>2</sub> > 1 is prevalent in the daytime atmosphere, sufficiently high HO<sub>2</sub>/RO<sub>2</sub> is crucial to mimic  
20 atmospheric conditions and to prevent biases by low HO<sub>2</sub>/RO<sub>2</sub> on the HOM product distribution and thus SOA yield.  
21 Experiments were performed under steady-state conditions in the new, continuously stirred tank reactor SAPHIR-STAR at  
22 Forschungszentrum Jülich. The HO<sub>2</sub>/RO<sub>2</sub> ratio was increased by adding CO, while keeping the OH concentration constant.  
23 We determined the HOM's SOA formation potential, considering their fraction remaining in the gas phase after seeding with  
24 (NH<sub>4</sub>)<sub>2</sub>SO<sub>4</sub> aerosol. Increase of HO<sub>2</sub>/RO<sub>2</sub> led to a reduction in SOA formation potential, with the main driver being a  $\approx 60$  %  
25 reduction in HOM-accretion products. We also observed a shift in HOM-monomer functionalization from carbonyl to  
26 hydroperoxide groups. We determined a reduction of the HOM's SOA formation potential by  $\approx 30$  % at HO<sub>2</sub>/RO<sub>2</sub>  $\approx 1/1$   
27 compared to HO<sub>2</sub>/RO<sub>2</sub>  $\approx 1/100$ . Particle phase observations measured an about according decrease in SOA mass and yield.  
28 Our study showed that too low HO<sub>2</sub>/RO<sub>2</sub> ratios compared to the atmosphere can lead to an overestimation of SOA yields.

## 29 1 Introduction

30 In the atmosphere highly oxidized products from the oxidation of biogenic or anthropogenic volatile organic compounds  
31 (VOCs) are an important source of secondary organic aerosol (SOA) (Roldin et al., 2019; Mohr et al., 2019). SOA is an  
32 important contributor to the overall ambient aerosol and of interest because of its impact on climate, visibility, and human  
33 health (Hallquist et al., 2009).

34 Recently, many studies (Pullinen et al., 2020; Berndt et al., 2016; Bianchi et al., 2017) have focused on understanding the  
35 oxidation pathways of VOCs that yield highly oxygenated molecules (HOMs), as these are expected to be of low enough  
36 volatility to condense into the particle phase. One important tool for the investigation of VOC degradation and SOA  
37 formation is the utilization of experiments in atmospheric simulation chambers (Hidy, 2019). Such experiments have also  
38 helped to elucidate key processes in the HOM formation, i.e. the process of autoxidation.

39 After an initial oxidant attack and the formation of a peroxy radical ( $\text{RO}_2$ ), autoxidation adds oxygen to the molecule via an  
40 internal H-shift to the peroxy group, forming a hydroxy peroxide group and an alkyl radical, to which  $\text{O}_2$  immediately adds,  
41 reestablishing the peroxy functionality. This process can be repeated multiple times yielding almost instantaneously highly  
42 oxygenated peroxy radicals ( $\text{HOM-RO}_2$ ) which are terminated to a series of HOM closed-shell products (Bianchi et al.,  
43 2019; Ehn et al., 2014; Crouse et al., 2013).

44 Chamber studies often work with a singular compound and operate at higher precursor concentrations than those observed in  
45 the atmosphere for experimental reasons. These experiments cannot represent the complex mixture of VOCs and oxidized  
46 VOCs present in the atmosphere (McFiggans et al., 2019). Higher precursor concentrations can lead per se to higher SOA  
47 yields than observed in the atmosphere (a well characterized phenomenon (see Henry et al. (2012), Shilling et al. (2009)) and  
48 to a general preference of higher order processes which may not be important in the atmosphere. One example is that  
49 chamber studies tend to overestimate the role of cross reactions between organic peroxy radicals ( $\text{RO}_2$ ) owing to high  
50 precursor concentrations of a single VOC. In chambers, reactions of  $\text{HOM-RO}_2$  with other organic peroxy radicals terminate  
51 the autoxidation chain, leading typically to multifunctional carbonyl and alcohol compounds. In comparison, in the  
52 atmosphere termination by  $\text{HO}_2$  is more likely, leading to multifunctional hydroperoxides. In presence of sufficient  $\text{NO}$ ,  
53 termination to multifunctional organic nitrates may be more important (Schervish and Donahue, 2021).

54 Another possible termination reaction of  $\text{HOM-RO}_2$  with  $\text{HOM-RO}_2$  and less oxidized  $\text{RO}_2$  leads to the formation of  
55 accretion products, which are expected to be extremely low volatile organic compounds (ELVOCs) and are therefore  
56 expected to contribute to new particle formation and SOA formation (Ehn et al., 2014; Berndt et al., 2018). Schervish and  
57 Donahue (2021) raised awareness that chamber studies could overestimate the SOA formation potential from the oxidation  
58 of terpenes such as  $\alpha$ -pinene compared to the atmosphere, because of missing  $\text{HO}_2$  and small  $\text{RO}_2$  (e.g.  $\text{CH}_3\text{O}_2$ ), which favors  
59 accretion product formation. Previous studies of VOC ozonolysis with different OH scavengers by Docherty and Ziemann  
60 (2003) and Keywood et al. (2004), indicated a significant impact of the  $\text{HO}_2/\text{RO}_2$  ratio on SOA yields.

61 In chamber studies the use of higher VOC concentrations is often an unavoidable necessity either to match the sensitivity of  
62 the analytical instrumentation or to overcome chamber related effects. The question remains, how can conditions dictated by  
63 the chamber be steered towards more realistic chemical pathways and higher atmospheric relevance?

64 In this study we address this overestimated importance of peroxy radical cross reactions. We studied the photooxidation of  $\alpha$ -  
65 pinene in a series of steady-state experiments in the newly built continuously stirred tank reactor SAPHIR-STAR (a  
66 modernized version of JPAC, see Mentel et al. (2009)).

67 We compared two experimental conditions, a pure  $\alpha$ -pinene photooxidation case leading to low HO<sub>2</sub>/RO<sub>2</sub> ratios and high  
68 importance of RO<sub>2</sub> cross-reactions and a high HO<sub>2</sub>/RO<sub>2</sub> case representing more atmospheric relevant conditions with high  
69 importance of RO<sub>2</sub> + HO<sub>2</sub> reactions. One important concept of the conducted experiments is the constant OH availability to  
70  $\alpha$ -pinene in order to prevent effects of different oxidant levels and allow for a direct comparison between the two chemical  
71 regimes. To this end, the OH concentration in the experiments was adjusted to keep the  $\alpha$ -pinene OH turnover constant and  
72 to avoid changes due to oxidant scavenging.

73 Furthermore, the addition of seed particles ((NH<sub>4</sub>)<sub>2</sub>SO<sub>4</sub>) allowed us to observe the condensation behavior of the HOM-  
74 products and to compare our gas phase observations directly with particulate phase measurements of the condensed organic  
75 mass.

76 In this study we will address two central questions: How does the shift in HO<sub>2</sub>/RO<sub>2</sub> impact the oxidation mechanism of  
77  $\alpha$ -pinene, especially the HOM formation pathway? And what is the subsequent impact on the SOA formation potential of the  
78  $\alpha$ -pinene photooxidation system? As the central analysis tool, we will use high resolution time of flight mass spectrometry  
79 with chemical ionization (HR-TOF-CIMS) with nitrate (NO<sub>3</sub><sup>-</sup>) reagent ions as this ionization scheme is selective towards  
80 HOM compounds (Hyttinen et al., 2018).

## 81 **2 Methods**

### 82 **2.1 Generic $\alpha$ -pinene HOM peroxy radical chemistry**

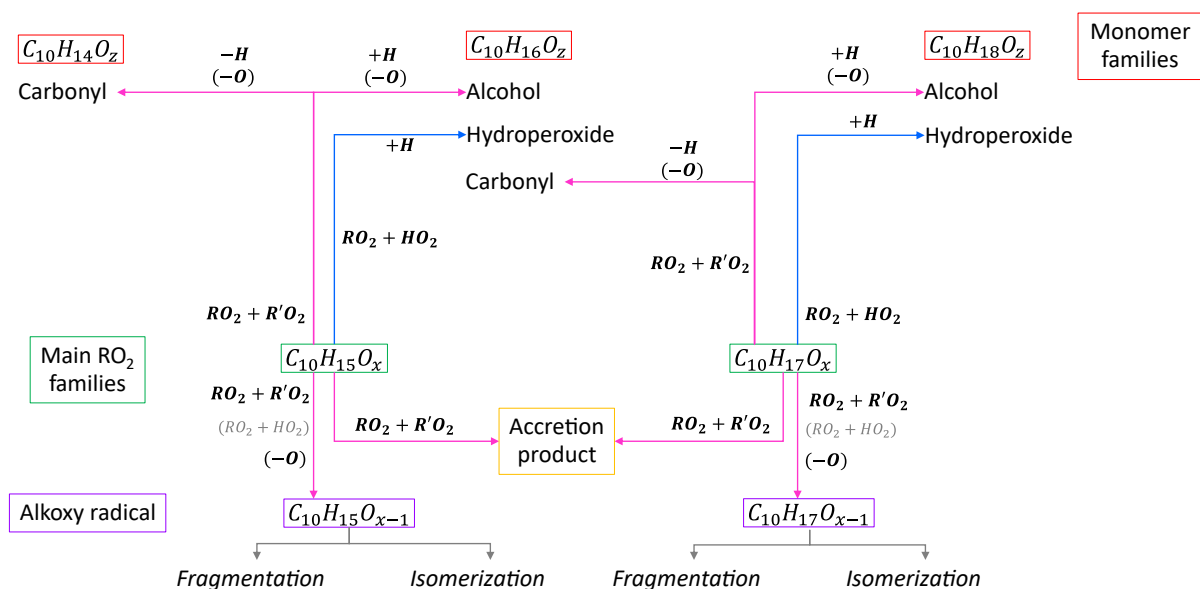
83 The chemical mechanistic information for the basic oxidation scheme of  $\alpha$ -pinene was taken from the Master Chemical  
84 Mechanism MCM v3.3.1 (Jenkin et al., 1997; Saunders et al., 2003) (<http://mcm.york.ac.uk>). The main peroxy radicals  
85 expected from  $\alpha$ -pinene photooxidation are C<sub>10</sub>H<sub>17</sub>O<sub>x</sub> and C<sub>10</sub>H<sub>15</sub>O<sub>x</sub>. C<sub>10</sub>H<sub>17</sub>O<sub>x</sub> is formed by the addition of OH to  $\alpha$ -pinene,  
86 followed by O<sub>2</sub> (starting RO<sub>2</sub>: C<sub>10</sub>H<sub>17</sub>O<sub>3</sub>) (MCM v3.3.1 (Jenkin et al., 1997; Saunders et al., 2003)). Studies showed that the  
87 autoxidation can start from C<sub>10</sub>H<sub>17</sub>O<sub>3</sub> with the four-member ring in  $\alpha$ -pinene opened (Berndt, 2021; Xu et al., 2019).

88 For C<sub>10</sub>H<sub>15</sub>O<sub>x</sub> the autoxidation chain is assumed to start with C<sub>10</sub>H<sub>15</sub>O<sub>4</sub>, which can be formed directly from ozonolysis via the  
89 vinyl hydroperoxide path (Johnson and Marston, 2008; Iyer et al., 2021) or via H-abstraction from first-generation oxidation  
90 products such as pinonaldehyde (C<sub>10</sub>H<sub>16</sub>O<sub>2</sub>). (MCM v3.3.1 (Jenkin et al., 1997; Saunders et al., 2003; Fantechi et al., 2002)).

91 A recent study suggests direct H-abstraction by OH from  $\alpha$ -pinene (Shen et al., 2022) as a starting point for the autoxidation  
 92 chain.

93 The autoxidation process is rapid with H-shift rates of about  $0.01 - 0.1 \text{ s}^{-1}$  and faster (Piletic and Kleindienst, 2022; Berndt,  
 94 2021; Xu et al., 2019; Vereecken et al., 2007). The autoxidation chain will run quickly, adding more oxygen to the molecule,  
 95 until bimolecular termination reactions are able to compete with all available H-shift rates. The rate of an H-shift is  
 96 determined by the hydrogen's position in relation to the peroxy radical and the functional groups near the hydrogen and  
 97 peroxy radical (Otkjaer et al., 2018; Vereecken and Nozière, 2020). In the absence of  $\text{NO}_x$ , the peroxy radicals have two  
 98 major bimolecular termination channels: the reaction with another  $\text{RO}_2$  or with  $\text{HO}_2$ . A third pathway is the intramolecular  
 99 termination (Rissanen et al., 2014).

100 Based on the considerations above, we apply a simplified generic reaction scheme to analyze our observations. **Figure 1**  
 101 shows an overview of the reaction pathways for the main peroxy radical families in the  $\alpha$ -pinene photooxidation and the  
 102 resulting product groups and families. The compounds can be separated into four classes; peroxy radicals (HOM- $\text{RO}_2$ ),  
 103 monomers (HOM-Mon), accretion products (HOM-Acc) and fragments (HOM-Frag). The HOM- $\text{RO}_2$  class consists of all  
 104 detected HOM- $\text{RO}_2$ , with special focus on the analysis of the  $\text{C}_{10}$  HOM- $\text{RO}_2$  family. The HOM-Mon class contains the  
 105 closed-shell HOM- $\text{C}_{10}$  products. The compounds in the fragment class contain less than ten carbon atoms, while all  
 106 HOM-Acc compounds contain more than ten carbon atoms. The compound classes are further divided into groups and  
 107 families. Here, the term group is used for compounds with the same carbon number, while a family contains all compounds  
 108 with the same carbon and hydrogen number but a varying oxygen number.



109

110 **Figure 1: Overview of important reaction pathways of  $\alpha$ -pinene  $\text{RO}_2$  with other  $\text{RO}_2$  and  $\text{HO}_2$ .**

111 The termination of RO<sub>2</sub> with HO<sub>2</sub> will lead to hydroperoxide formation:



112 In the case of C<sub>10</sub>H<sub>15</sub>O<sub>x</sub>, reaction (**R1**) will lead to multifunctional C<sub>10</sub>H<sub>16</sub>O<sub>z</sub> hydroperoxides (wherein the notation  
113 “hydroperoxides” or “carbonyls”, “alcohols” etc. here and in the following relates to the functionality of the group formed by  
114 the termination reaction). For C<sub>10</sub>H<sub>17</sub>O<sub>x</sub> it will lead to the formation of C<sub>10</sub>H<sub>18</sub>O<sub>z</sub> hydroperoxides. The termination via  
115 RO<sub>2</sub>+RO<sub>2</sub> can either result in the formation of accretion products or in the formation of carbonyls and alcohols. For the  
116 accretion product formation, it is assumed that the two RO<sub>2</sub> chemically bond eliminating O<sub>2</sub> from the molecule:



117 Recombination reactions of the main peroxy radical families C<sub>10</sub>H<sub>15</sub>O<sub>x</sub> and C<sub>10</sub>H<sub>17</sub>O<sub>x</sub> lead to the product families C<sub>20</sub>H<sub>30</sub>O<sub>z</sub>  
118 (combination of two C<sub>10</sub>H<sub>15</sub>O<sub>x</sub>), C<sub>20</sub>H<sub>32</sub>O<sub>z</sub> (combination of C<sub>10</sub>H<sub>15</sub>O<sub>x</sub> and C<sub>10</sub>H<sub>17</sub>O<sub>x</sub>), and C<sub>20</sub>H<sub>34</sub>O<sub>z</sub> (combination of two  
119 C<sub>10</sub>H<sub>17</sub>O<sub>x</sub>).

120 However, due to reactions with smaller peroxy radicals, HOM-Acc families with smaller carbon and hydrogen numbers are  
121 also observed. Indeed, one reason why the RO<sub>2</sub>+R'O<sub>2</sub> termination is expected to affect the SOA formation potential is the  
122 formation of accretion products by scavenging of less oxidized and smaller RO<sub>2</sub> by HOM-RO<sub>2</sub>. Thus, the smaller RO<sub>2</sub> will  
123 also contribute to the SOA mass which would otherwise not be the case. For the HOM-RO<sub>2</sub> itself, it is expected that they  
124 contribute to SOA formation independently of the termination pathway, due to the low volatility of its expected termination  
125 products (Pullinen et al., 2020; McFiggans et al., 2019).

126 The second RO<sub>2</sub>+R'O<sub>2</sub> termination pathway is the formation of a carbonyl and alcohol compound:



127 In this reaction both radicals lose an oxygen atom, and a hydrogen atom is transferred to the RO<sub>2</sub> forming the alcohol  
128 termination group. Preferences of RO<sub>2</sub> to form an alcohol or carbonyl compound are possible for individual reactions, but  
129 statistically carbonyl and alcohols should be formed with the same fractions. Since mass spectrometry can only determine  
130 formula composition, we cannot distinguish alcohols and hydroperoxides, which arise from RO<sub>2</sub> differing by one O atom.  
131 Therefore, details of balance of alcohol and carbonyl formation cannot be detected.

132 However, the formula composition can help to differentiate certain formation pathways. The C<sub>10</sub>H<sub>14</sub>O<sub>z</sub> family contains only  
133 carbonyl formed from a C<sub>10</sub>H<sub>15</sub>O<sub>x</sub> RO<sub>2</sub> while the alcohol will be part of the C<sub>10</sub>H<sub>16</sub>O<sub>z</sub> family. The C<sub>10</sub>H<sub>16</sub>O<sub>z</sub> family also  
134 contains the carbonyl produced from the RO<sub>2</sub>+R'O<sub>2</sub> monomer termination of C<sub>10</sub>H<sub>17</sub>O<sub>x</sub>, while the alcohol from this RO<sub>2</sub>  
135 family will be found in the C<sub>10</sub>H<sub>18</sub>O<sub>z</sub> family. So, from a diagnostic point of view, C<sub>10</sub>H<sub>14</sub>O<sub>z</sub> as well as C<sub>10</sub>H<sub>18</sub>O<sub>z</sub> are uniquely  
136 related to a precursor radical family.

137 The classification of the formation pathways of the monomers is helpful to analyze the effect of the HO<sub>2</sub>/RO<sub>2</sub> ratio shift in  
138 the experiments. Considering the termination pathways, a decrease in the C<sub>10</sub>H<sub>14</sub>O<sub>z</sub> family and an increase of the C<sub>10</sub>H<sub>18</sub>O<sub>z</sub>  
139 family is expected with increasing HO<sub>2</sub>/RO<sub>2</sub> because of increasing termination by HO<sub>2</sub> and decreasing termination by RO<sub>2</sub>.  
140 In case of C<sub>10</sub>H<sub>18</sub>O<sub>z</sub> the increase of hydroperoxides is partially compensated by a decrease of the alcohol channel. For  
141 C<sub>10</sub>H<sub>16</sub>O<sub>z</sub> the situation is more complicated as it contains contributions from all termination pathways.

142 Besides closed-shell products, HOM-RO<sub>2</sub> can also form alkoxy radicals (HOM-RO). In general, alkoxy radicals (RO) are  
143 important intermediates in the oxidation scheme of organics and are formed via (**R4**) and probably also via (**R5**) for specific  
144 RO<sub>2</sub> (Jenkin et al., 2019):



145 In reaction (**R5**) OH will be formed. The importance of reaction (**R5**) compared to reaction (**R1**) is still unclear in the  
146 literature, but functionalization of the RO<sub>2</sub> close to the peroxy functionality possibly enables this reaction (Iyer et al., 2018;  
147 Eddingsaas et al., 2012; Hasson et al., 2005; Jenkin et al., 2019). If reaction (**R5**) is of negligible importance, the reaction  
148 scheme will simplify and the effect of increased HO<sub>2</sub>/RO<sub>2</sub> is easier to diagnose.

149 We are interested in the importance of alkoxy radical formation as (HOM)-RO tend to fragment, leading to the formation of  
150 smaller products (Vereecken et al., 2007). In the context of SOA formation, these fragments are less likely to contribute to  
151 SOA mass because of their higher volatility. Since alkoxy radicals are too unstable to be detected directly we use two  
152 diagnosis tools to judge the importance of HOM-RO. Firstly, HOM-RO fragmentation can lead to HOM-RO<sub>2</sub> with less than  
153 10 carbon atoms which may also continue the autoxidation chain. Therefore, the abundance of HOM with less than 10  
154 carbon atoms (HOM-Frag) indicates the importance of alkoxy steps. Secondly, with increasing functionalization, H-shifts  
155 retaining the carbon backbone become more likely (Vereecken et al., 2007) which will lead to a next generation of C<sub>10</sub>-  
156 HOM-RO<sub>2</sub>. Such alkoxy peroxy steps can continue the autoxidation chain (Mentel et al., 2015). Interestingly, by coupling of  
157 an alkoxy and a peroxy step, the parity of the number of oxygen atoms in the HOM-RO<sub>2</sub> changes, while in pure autoxidation  
158 steps the oxygen parity remains the same. Therefore, a parity change of the oxygen number can be used as an indication of  
159 alkoxy step abundance (Kang, 2021).

160 In summary we will use the changes in contribution and relative signal of the different families and classes to judge the  
161 impact of shifting from low to high HO<sub>2</sub>/RO<sub>2</sub> on the α-pinene photooxidation pathway.

## 162 **2.2 Control of α-pinene OH turnover**

163 After the initial α-pinene photooxidation phase as a reference, CO was added to the oxidation system. The idea is to  
164 represent small, oxidized VOCs in the atmosphere that can produce HO<sub>2</sub> by reaction with OH (compare Schervish and

165 Donahue (2021)). Presence of CO shifts the HO<sub>2</sub> to RO<sub>2</sub> ratio, increasing the importance of the termination of RO<sub>2</sub> by HO<sub>2</sub>.  
166 McFiggans et al. (2019) showed that one limiting factor in mixture experiments is oxidant scavenging: the products and their  
167 yields in mixed systems change, because there is less OH available to the individual VOC. Thus, after the CO addition the  
168 OH production in the chamber was increased to compensate for the OH consumed by CO. The OH levels in the system  
169 before and after the CO addition were approximately the same, keeping the  $\alpha$ -pinene OH turnover approximately constant.  
170 This OH adjustment ensures that the primary  $\alpha$ -pinene chemistry was kept the same, avoiding effects by different oxidant  
171 levels, and enabling a direct comparison.

172 However, since experiments could only be performed at *about* the same OH levels, a normalization by the actual  $\alpha$ -pinene  
173 OH turnover is applied to the data. This compensates for the slight experimental imperfections and enables better  
174 comparison of experiment series with different boundary conditions. The turnover in steady state is given in **Eq. (1)**. Here  
175 the subscript “SS” denotes steady state condition for the concentrations of  $\alpha$ -pinene and OH,  $k_{OH}$  is the  $\alpha$ -pinene OH reaction  
176 rate constant.

$$turnover_{\alpha\text{-pinene}+OH} = k_{OH} * [\alpha\text{-pinene}]_{SS} * [OH]_{SS} \quad (1)$$

177 This normalization also directly shows the yield of certain oxidation product or product group per  $\alpha$ -pinene consumed by  
178 OH.

### 179 **2.3 Derivation of effect on condensable mass from gas-phase measurement**

180 A simple proxy for the condensable mass from HOM products can be calculated from the steady-state HOM-signals  
181 measured by the NO<sub>3</sub>-CIMS, assuming condensation for all low volatility HOM-compounds and no back evaporation into  
182 the gas phase. To only take low volatility products into account we used all detected formula compositions with  
183  $M > 230 \text{ g mol}^{-1}$  and weighted them with their molar mass. The reasoning behind this threshold can be found in **Sect. 4.4**. All  
184 contributions were summed up and normalized with the  $\alpha$ -pinene OH turnover for the comparison between the low and high  
185 HO<sub>2</sub>/RO<sub>2</sub> cases (**Eq. (2)**).

$$mass\ weighted\ signal\ sum = \frac{\sum_{i=0}^i S_i * M_i}{turnover_{\alpha\text{-pinene}+OH}} \quad (2)$$

186 We also estimated the expected SOA mass formed using the calibration factor obtained for sulfuric acid for our NO<sub>3</sub>-CIMS  
187 instrument in a calibration setup (see supplement **Sect. S1**). From this we calculated an upper boundary concentration of  
188 detected HOM-compounds in the gas phase under the assumption that sulfuric acid clusters with nitrate at the collision limit,  
189 yielding maximum sensitivity (a common approach, see for example Ehn et al. (2014), Pullinen et al. (2020)).

190 The calculated gas phase concentration was then used in the steady state equation describing the relationship between gas  
191 and particle phase concentrations of a single compound  $i$  shown in **Eq. (3)**.

$$m_{i,seed}(p) = \frac{m_{i,seed}(g) * k_{cond,i}}{k_{particleLoss} + k_{evap,i}} \quad (3)$$

192 **Equation (3)** shows that the steady state particle phase (mass) concentration  $m_{i,seed}(p)$  of compound  $i$  in presence of seed in  
 193 the chamber is only dependent on the steady state gas phase concentration  $m_{i,seed}(g)$ , the condensation rate and evaporation  
 194 rate constants  $k_{cond,i}$ ,  $k_{evap,i}$  of  $i$  (to and from the particles) and the particle loss rate constant  $k_{particleLoss}$  in the chamber.  
 195 The condensation rate can be calculated (see supplement **Sect. S8**), and the particle loss rate constant was measured by  
 196 observation of the particle loss in the chamber after ending the seed addition (details in the supplement **Sect. S2**). The  
 197 evaporation rate was assumed to be negligible for the investigated HOM-compounds.  
 198 For the SOA yield calculation, we calculate a corrected organic mass  $m_{SOA}$  from the organic mass  $m_{AMS}$  measured by aerosol  
 199 mass spectrometry (AMS) and the fraction expected to be lost on the seed particles compared to the overall loss on particles  
 200 and chamber wall as shown in **Eq. (4)** (McFiggans et al., 2019).

$$m_{SOA} = m_{AMS} * \frac{k_{cond} + k_{wall}}{k_{cond}} \quad (4)$$

201 In **Eq. (4)** we use the condensation rate constant  $k_{cond}$  calculated for one major HOM-product ( $C_{10}H_{16}O_7$ ) and the average  
 202 HOM-Mon wall loss rate  $k_{wall}$  which was determined by switching off the UVC light and observing the decay of  
 203 photooxidation products in the  $NO_3$ -CIMS. The wall loss determination, as well as SOA mass correction were described  
 204 before in Sarrafzadeh et al. (2016) and McFiggans et al. (2019).

## 205 3 Experimental methods

### 206 3.1 Chamber setup

207 Experiments were conducted in the Jülich SAPHIR STAR chamber, which is the modern successor of the JPAC setup  
 208 (Mentel et al., 2009). The basic concepts are the same as in JPAC, but each parameter is set, controlled, and monitored in a  
 209 program. The chamber was operated as a continuously stirred tank reactor. It is a borosilicate glass cylinder (l=2.5 m, d=1 m)  
 210 with a volume of close to 2000 L and all equipment inside the chamber is either glass or glass coated steel (SilcoTek  
 211 GmbH).

212 With an inflow of  $32 \text{ L min}^{-1}$ , the residence time in the chamber was approximately 61 minutes with a fan ensuring mixing  
 213 within minutes. In contrast to the JPAC chamber, the stirring is conducted perpendicular to the cylinder axis, as opposed to  
 214 coaxial. Chamber inflow is split into two humidified clean air flows (mixed from  $N_2$  and  $O_2$ ) of about equal volume, one  
 215 with added oxidant (here  $O_3$ ), the other with added VOC and other trace gases (here  $\alpha$ -pinene and CO). All experiments were  
 216 performed at a relative humidity of 50 % and at 20 °C. Temperature stability is ensured by the climate-controlled  
 217 surrounding of the chamber.



218  $\alpha$ -Pinene ( $\geq 99$  % purity, Sigma-Aldrich Merck KGaA) was introduced via liquid injection with a syringe pump (Fusion  
219 4000, CHEMYX Inc.) into a heated glass bulb and flushed by a stream of  $1 \text{ L min}^{-1}$  into the chamber. CO was added from a  
220 gas bottle (10 % CO in  $\text{N}_2$ , Messer SE & Co. KGaA). Ozone was directly produced photolytically before injection with a  
221 self-built ozone generator.

222 OH is produced in the chamber by ozone photolysis using two UV-C lamps with a wavelength of 254 nm and subsequent  
223 reaction of  $\text{O}(^1\text{D})$  with water vapor. The lamps are mounted in closed quartz cylinders in the middle of the chamber,  
224 vertically to the cylinder axis and light intensity can be varied with a movable shielding installed around the lamps. The  
225 shielding allows an exact percentage of the lamp to be covered, thus controlling the amount of OH produced in the chamber.

226 The OH radical concentration after CO addition was adjusted by setting the shielding of the UVC lamps and a slight  
227 adjustment of  $\text{O}_3$  inflow. The applied  $J(\text{O}^1\text{D})$  values in different phases were calculated to be in the range of  $0.8 \cdot 10^{-3}$  to  
228  $2.4 \cdot 10^{-3} \text{ s}^{-1}$ .

229 In some of the experiments, ammonium sulfate ( $\geq 99$  % purity, Merck KGaA) seed particles were added to the system to  
230 provide a surface for the condensation of organic material. The aerosol was produced with a modified TSI atomizer (Model  
231 3076, TSI GmbH) and dried to 50 % relative humidity.

232 VOC concentrations in the chamber were measured using proton-transfer-reaction mass spectrometry (PTR-TOF-MS;  
233 Ionicon GmbH).  $\text{CO}_2$ , CO,  $\text{H}_2\text{O}$  (G2401 Cavity Ringdown Spectrometer, Picarro Inc.), NO,  $\text{NO}_x$  (NCLD899, Eco Physics  
234 GmbH with a home-built photolytic converter) and  $\text{O}_3$  (O342e, Envea GmbH) were additionally monitored. Particle  
235 distribution and concentration were measured with a condensation particle counter (CPC, Model 3788, TSI GmbH) and a  
236 scanning mobility particle sizer (SMPS; Model 3080, TSI GmbH) with a CPC (Model 3788, TSI GmbH). The aerosol  
237 composition was measured with a high-resolution aerosol mass spectrometer (HR-TOF AMS; Aerodyne Inc.).

238 In all experiments, VOC,  $\text{O}_3$ , and SMPS+CPC sampling switched between inlet and outlet of the chamber to measure the  
239 input concentrations as well as the concentrations in the reactor. The flow control system of the chamber adapts to these  
240 switches so that the inflow into the chamber stays constant.

241 All results discussed here were observed under steady-state conditions when all parameters were constant. For each steady  
242 state, the OH concentration was calculated from the decay of  $\alpha$ -pinene as described by Kiendler-Scharr et al. (2009).  
243 **Equation (5)** is derived from the mass balance of  $\alpha$ -pinene at steady state. The steady state OH concentration  $[\text{OH}]_{\text{SS}}$   
244 depends on the amount of  $\alpha$ -pinene consumed by reaction with OH and the reaction with  $\text{O}_3$ , as well as the flush out.

$$[\text{OH}]_{\text{SS}} = \frac{F}{V} * \frac{[\text{VOC}]_{\text{in}} - [\text{VOC}]_{\text{SS}} - k_{\text{O}_3} * [\text{O}_3]_{\text{SS}}}{k_{\text{OH}}} \quad (5)$$

245 Here, F is the total flow and V the volume of the chamber. The subscript “SS” indicates steady-state concentrations, while  
246  $[\text{VOC}]_{\text{in}}$  represents the  $\alpha$ -pinene concentration entering the chamber.  $k_{\text{O}_3}$  and  $k_{\text{OH}}$  represent the reaction rate constants of  $\alpha$ -

247 pinene with the corresponding oxidant. We applied rate coefficients of  $k_{OH}=5.36 \cdot 10^{-11} \text{ cm}^3 \cdot \text{s}^{-1}$  (Atkinson and Arey, 2003) and  
 248  $k_{O_3}=9.25 \cdot 10^{-17} \text{ cm}^3 \cdot \text{s}^{-1}$  (Cox et al., 2020) at 20 °C. The uncertainty of the OH calculation was estimated as 20 % by Wildt et  
 249 al. (2014).

### 250 3.2 Experiment conditions

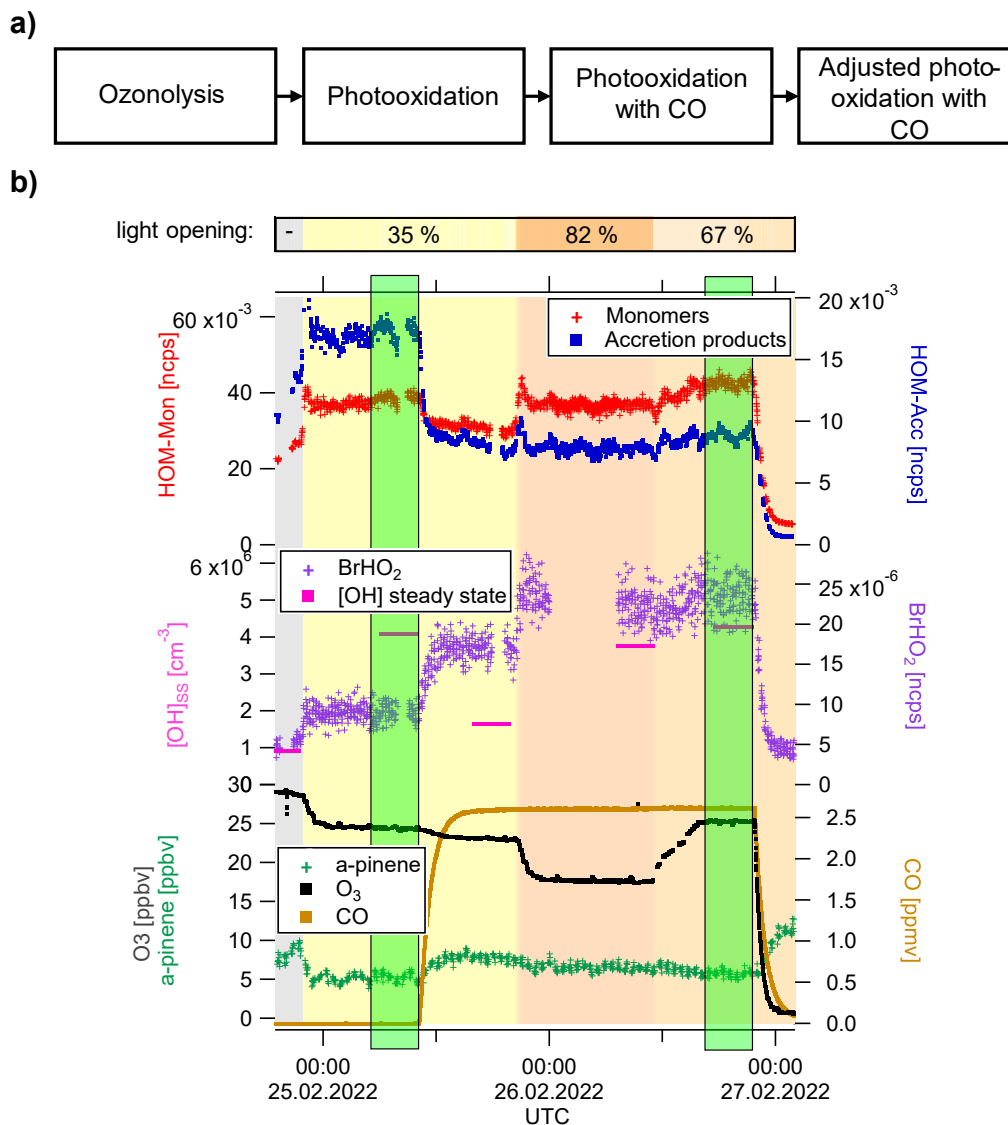
251 An overview of the experiments and their boundary conditions can be found in **Table 1**. Four experiments were performed  
 252 in total, leading to one repetition of each studied condition. In two of the experiments ammonium sulfate seeds were added  
 253 leading to a total particle surface in the chamber on the order of  $8 \cdot 10^{-4} \text{ m}^2 \text{ m}^{-3}$  and organic loadings of about  $3 \text{ } \mu\text{g m}^{-3}$  in the  
 254 photooxidation stage. In the unseeded experiments no significant nucleation was observed leading to pure gas phase  
 255 conditions. The Exp2 experiment is a consecutive combination of a seeded, followed by a non-seeded experiment to provide  
 256 direct insight into the effect of seed presence on the system.

257 As the OH radical is produced by photolysis of ozone and  $\alpha$ -pinene reacts with ozone, it is important to know the relative  
 258 contribution of the  $\alpha$ -pinene consumption by OH and by  $O_3$ . This is achieved by comparing the turnover of  $\alpha$ -pinene with  
 259 OH and  $O_3$  respectively. The results can be found in **Table 1**. The listed results are for the low  $HO_2/RO_2$  conditions, but  
 260 nearly identical values were reached after the  $HO_2/RO_2$  shift.

261 **Table 1. Overview of experimental conditions**

Name	Experiment description	[VOC] <sub>in</sub>	[CO] <sub>in</sub>	[OH] <sub>ss</sub> at low $HO_2/RO_2$	Contribution of OH to turnover at low $HO_2/RO_2$	Particle surface at low $HO_2/RO_2$	Organic mass concentration at low $HO_2/RO_2$
<u>Exp1</u>	<i>unseeded (1)</i>	10 ppbv	2.5 ppmv	4.8E+6 $\text{cm}^{-3}$	80 %	-	-
<u>Exp2.1</u>	<i>seeded (1)</i>	10 ppbv	2.5 ppmv	1.1E+7 $\text{cm}^{-3}$	92 %	8.7E-4 $\text{m}^2 \text{ m}^{-3}$	3.4 $\mu\text{g m}^{-3}$
<u>Exp2.2</u>	<i>unseeded (2)</i>	10 ppbv	2.5 ppmv	1.5E+7 $\text{cm}^{-3}$	94 %	-	-
<u>Exp3</u>	<i>seeded (2)</i>	10 ppbv	2.5 ppmv	1.1E+7 $\text{cm}^{-3}$	92 %	6.8E-4 $\text{m}^2 \text{ m}^{-3}$	2.7 $\mu\text{g m}^{-3}$

262



264

265 **Figure 2: a) Experiment flow scheme b) Exemplary timeseries of *ExpI* experiment showing HOM-Mon and HOM-Acc**  
 266 **product sum (top panel), calculated OH concentration and BrHO<sub>2</sub> signal (middle panel), and ozone, α-pinene and CO**  
 267 **concentrations (bottom panel). Background color represents light intensity. Highlighted in green are the low HO<sub>2</sub>/RO<sub>2</sub>**  
 268 **steady state and the steady state at high HO<sub>2</sub>/RO<sub>2</sub> (addition of CO and adjusted oxidant level).**

269 All experiments started with α-pinene ozonolysis followed by illumination of the UVC-lights to induce the reaction with  
 270 OH. A general flow scheme of the experiment can be found in **Fig. 2**, together with one exemplary timeseries of the  
 271 unseeded experiment *ExpI*. After the photooxidation steady state, CO was added to the system. In the displayed *ExpI* the  
 272 OH level was adjusted in three steps to approach the same concentration as before the CO addition. First the UVC-light  
 273 opening was adjusted and then O<sub>3</sub> was added, and the UVC-light opening was adjusted again. In some experiments initially

274 the effect of CO on the unchanged system was observed, before the adjustment of OH. In other experiments (*Exp2.2*, *Exp3*)  
275 the adjustment of the  $\alpha$ -pinene OH turnover via ozone concentration and UVC-light opening were made simultaneously with  
276 the CO addition. Highlighted in green are the steady states with the “same” OH concentration characterized by low and high  
277  $\text{HO}_2/\text{RO}_2$ , which were used for analysis and interpretation.

### 278 **3.4 Model calculation for $\text{HO}_2/\text{RO}_2$ ratio estimation**

279 Box model calculations were performed applying the MCM v3.3.1 chemistry (Jenkin et al., 1997; Saunders et al., 2003)  
280 under the boundary conditions of the SAPHIR-STAR chamber. All calculations were performed with the institute software  
281 package EASY which uses FACSIMILE to solve the differential equations (EASY Version 5.69b). More details about the  
282 model parameters can be found in the supplement **Sect. S3**. The model calculations reproduced the primary observables  
283  $\alpha$ -pinene,  $\text{O}_3$ , CO, and OH within the experimental uncertainties. The box-model results were used to characterize the  
284  $\text{HO}_2/\text{RO}_2$  ratio of the chemical systems, as no direct measurement of these parameters was available. The observed cluster  
285 signal  $\text{BrHO}_2^-$  follows the modelled  $\text{HO}_2$  concentration (**Fig. 3**).

286 The model predicts a shift of the  $\text{HO}_2/\text{RO}_2$  ratio from about 0.01 to about 1 by CO addition and oxidant adjustment, an  
287 increase by two orders of magnitude. Owing to lack of observations to verify model results, we will consider only the  
288 magnitude of  $\text{HO}_2/\text{RO}_2$  here. The model results show that indeed a major shift from  $\text{RO}_2+\text{RO}_2$  to  $\text{RO}_2+\text{HO}_2$  reactions can be  
289 expected.

290 We further used the modelled  $\text{RO}_2$  and  $\text{HO}_2$  concentrations to estimate the relative importance of pathways for individual  
291 (observed) HOM- $\text{RO}_2$ . For that we applied two generic rate coefficients  $k_{\text{RO}_2\text{HO}_2}$  and  $k_{\text{RO}_2\text{RO}_2}$ . As the rate coefficient for the  
292  $\text{RO}_2+\text{HO}_2$  termination to a hydroperoxide  $k_{\text{RO}_2\text{HO}_2}$  we used the value specified in the MCM ( $2.46 \cdot 10^{-11} \text{ cm}^3 \cdot \text{s}^{-1}$  at  $20^\circ \text{C}$   
293 (Jenkin et al., 1997; Saunders et al., 2003)). We chose a  $k_{\text{RO}_2\text{RO}_2}$  of  $5 \cdot 10^{-12} \text{ cm}^3 \cdot \text{s}^{-1}$  as the approximated reaction rate of the  
294  $\text{RO}_2+\text{RO}_2$  reactions. This value applies to all possible reactions (accretion product, monomer, and alkoxy formation) and is  
295 in the range of  $k_{\text{RO}_2\text{RO}_2}$  utilized by Roldin et al. (2019) in the PRAM model.

### 296 **3.5 Determination of oxidized VOCs, HOMs and $\text{HO}_2$**

297 Chemical ionization mass spectrometry (HR-TOF-CIMS) techniques were used to detect a range of gaseous compounds. For  
298 this, two atmospheric pressure interface time of flight mass spectrometers (APi-TOF-MS; Tofwerk AG) with different inlet  
299 systems were used simultaneously. General information about the APi-TOF-MS instrument can be found in Junninen et al.  
300 (2010).

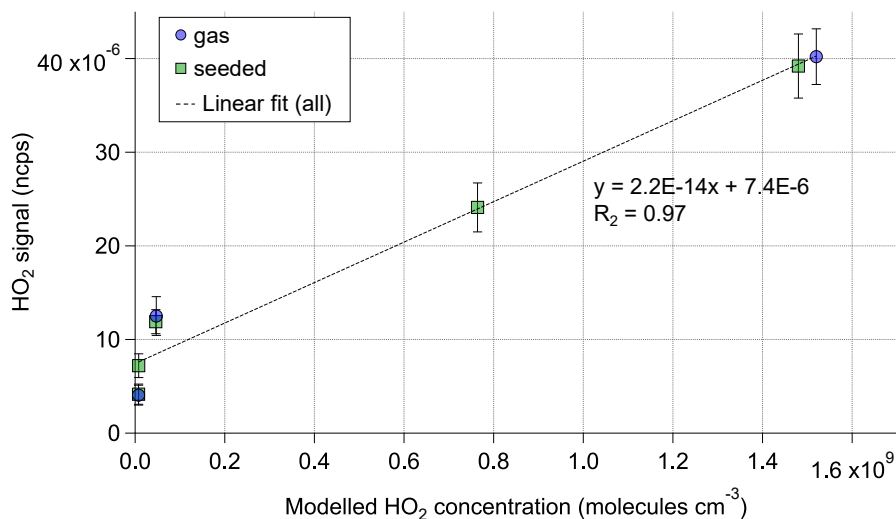
301 A long TOF (LTOF) (Resolution  $\sim 8500$  for peaks at  $>200 \text{ m/Q}$ ) was coupled with the multi-scheme ionization inlet (MION;  
302 Karsa Oy). The setup of the inlet is described in detail by Rissanen et al. (2019). The distinctive feature of the MION inlet is  
303 the switching between two reagent ions. Here, nitrate was used to detect closed-shell HOMs, as well as HOM- $\text{RO}_2$ . Bianchi  
304 et al. (2019) suggested to define HOM as products stemming from autoxidation containing more than 6 oxygen. In our

305 overall analysis we decided to also include fragments and monomers containing 5 or in a few cases 4 oxygens (see peaklist  
306 in supplement **Sect. S5**) as we are interested to see if the importance of these less oxidized (but still with NO<sub>3</sub>-CIMS  
307 detectable) products increases at higher HO<sub>2</sub>/RO<sub>2</sub>. However, in all considerations regarding SOA formation we furthermore  
308 set a molar weight threshold which automatically excluded any products with less 6 oxygens.

309 As the second reagent ion, bromide was used to detect less oxidized products and the HO<sub>2</sub> radical (Albrecht et al., 2019;  
310 Sanchez et al., 2016). The nitrate ion source had a reaction time of 600 ms, while the bromide ion source had a shorter  
311 reaction time of 60 ms. For all experiments an inlet flow of 10 L min<sup>-1</sup> was used and the ionization scheme was switched  
312 every 10 minutes.

313 In the data evaluation the first step was the separation of the timeseries of the two reagent ions. The data was subsequently  
314 processed with Tofware (Version 3.2.3, Tofwerk AG) using the high resolution timeseries workflow. No transmission  
315 correction was performed as previous measurements showed an approximately flat relative transmission curve in the mass  
316 region of interest. The analyte signals were normalized with the reagent ion signal (NO<sub>3</sub><sup>-</sup> and HNO<sub>3</sub>NO<sub>3</sub><sup>-</sup> for nitrate and Br<sup>-</sup>  
317 and BrH<sub>2</sub>O<sup>-</sup> for bromide).

318 Since no direct HO<sub>2</sub> calibration was available, the HO<sub>2</sub> signal in the Br-MION-CIMS was used to compare the levels of HO<sub>2</sub>  
319 relative to each other in the different phases of the experiment. The comparison of the measured HO<sub>2</sub> signal to the modelled  
320 HO<sub>2</sub> concentration shows a good linear relation between the model predictions and observations.



321

322 **Figure 3: Modelled HO<sub>2</sub> concentration vs. normalized HO<sub>2</sub> signal for each steady state of Exp2. HO<sub>2</sub> is measured as the BrHO<sub>2</sub>**  
323 **cluster and is normalized with the sum of the reagent ion Br<sup>-</sup> and its water cluster. The dotted line shows the linear fit to all (gas**  
324 **phase and seeded) measurement points.**

325 **Figure 3** illustrates this for the example of the Exp2 experiment. A background signal of around ~1·10<sup>-5</sup> is observed as soon  
326 as VOC and ozone are present in the reactor. The background HO<sub>2</sub> signal was not observed when only O<sub>3</sub> or only VOC were

327 in the system. As shown by the MCM modelling results HO<sub>2</sub> production of this strength is not expected in the  $\alpha$ -pinene  
328 ozonolysis phase but this background phenomenon was observed before (Albrecht et al., 2019) and is not fully understood.

329 For the HOM molecules measured by the NO<sub>3</sub>-MION-CIMS the relative changes between different experiment phases are  
330 compared. For all detected HOM products the same detection sensitivity is assumed. Hyttinen et al. (2018) showed in  
331 quantum chemical calculations that HOMs containing 6 or more oxygen atoms have comparable sensitivity with the nitrate  
332 reagent ion. At this degree of oxidation it can be expected that the HOMs already contain multiple hydroperoxyl and/or  
333 hydroxy functional groups (Bianchi et al., 2019) prior to the termination step, making it unlikely that the sensitivity is  
334 strongly influenced by the termination group. Thus, the signal strength reflects the correct ranking of the observations and  
335 relative comparisons do not require calibration. Pullinen et al. (2020) studied the mass balance between condensable HOMs  
336 and formed particle mass and were able to find closure within a factor of 2.

337 A second CI-APi-TOF was used to measure less oxidized species. It was configured with a CI inlet based on the design of  
338 Eisele and Tanner (1993) coupled to an HTOF (Resolution ~2700 for peaks at >200 m/Q) (ToFwerk AG) and was operated  
339 in positive mode with propylamine (C<sub>3</sub>H<sub>7</sub>NH<sub>2</sub>, Sigma-Aldrich, purity  $\geq 99\%$ ) to detect the early generation RO<sub>2</sub> and  
340 oxidation products (Berndt et al., 2018). The propylamine was purified and added as an amine-N<sub>2</sub> mixture (flow:  
341 0.12 mL min<sup>-1</sup>) to the 30 L min<sup>-1</sup> sheath flow. Furthermore, the sheath flow air is humidified to optimize ionization. The  
342 instrument sampled 0.1 L min<sup>-1</sup> from the chamber, which was diluted with 9.9 L min<sup>-1</sup> for a sample flow of 10 L min<sup>-1</sup>. The  
343 dilution was necessary to reduce depletion of the primary ion (Hantschke, 2022).

#### 344 **4 Results and Discussion**

345 In order to understand the effect of HO<sub>2</sub>/RO<sub>2</sub> on the gas phase product composition, we will present and compare two cases:  
346 The steady state without CO (low HO<sub>2</sub>/RO<sub>2</sub>) and the steady state with CO addition and OH adjustment by J(O<sup>1</sup>D) and O<sub>3</sub>  
347 (high HO<sub>2</sub>/RO<sub>2</sub>). The modelling results predicted HO<sub>2</sub>/RO<sub>2</sub> of about 1/100 and of about 1/1 for these two cases respectively.  
348 The modelled concentrations can be found in supplement **Sect. S4**. The modelling results show that the HO<sub>2</sub>/RO<sub>2</sub> ratio  
349 changes by two orders of magnitude, because [RO<sub>2</sub>] was reduced by about a factor of three, while [HO<sub>2</sub>] was increased by a  
350 factor of 30. Consequently, HO<sub>2</sub> reactions were almost negligible at low HO<sub>2</sub>/RO<sub>2</sub> while RO<sub>2</sub>+RO<sub>2</sub> reactions can still  
351 contribute at high HO<sub>2</sub>/RO<sub>2</sub>.

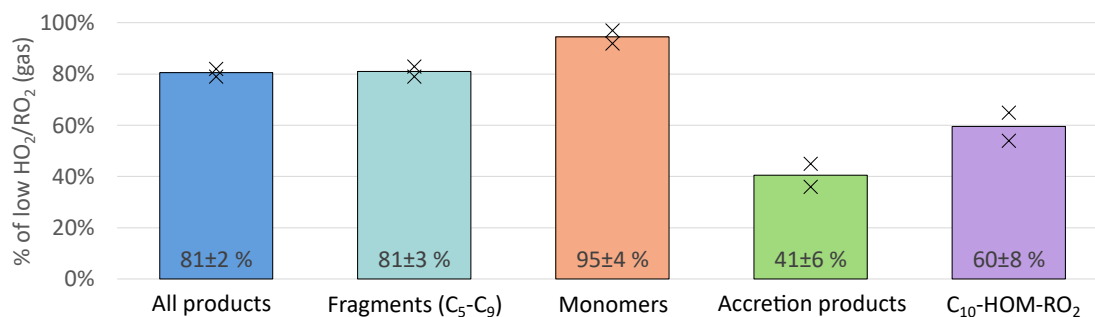
352 HO<sub>2</sub>/RO<sub>2</sub> ratios of around 1 are highly relevant for atmospheric conditions with significant OH oxidation, though it should  
353 be kept in mind that in atmospheric conditions the methyl peroxy radical and other small RO<sub>2</sub> contribute a significant portion  
354 to the total of peroxy radicals (Khan et al., 2015). Field studies reporting HO<sub>2</sub> and RO<sub>2</sub> measurements for different  
355 environments can be found in supplement **Table S5**. These exemplary studies show that HO<sub>2</sub>/RO<sub>2</sub> ratios around 1 are  
356 relevant in remote to urban environments with different VOC sources and NO<sub>x</sub> levels.

357 Assuming correctly modelled  $[\text{HO}_2]$  and  $[\text{RO}_2]$ , we calculated the competition between  $\text{HO}_2$  and  $\text{RO}_2$  reactions for each  
358 (observed)  $\text{RO}_2$  expressed in form of pseudo first order rate coefficients in  $k_{\text{RO}_2\text{HO}_2} \cdot [\text{HO}_2]$  or  $k_{\text{RO}_2\text{RO}_2} \cdot [\text{RO}_2]$ . Herein  
359  $[\text{RO}_2]$  is the sum of all  $\text{RO}_2$  species as defined in the MCM v3.3.1. For all experiments the results of our calculations indicate  
360 that the sink for  $\text{HOM-RO}_2$  is dominated by  $\text{RO}_2+\text{RO}_2$  reactions at low  $\text{HO}_2/\text{RO}_2$  (~97 % contribution), while at high  
361  $\text{HO}_2/\text{RO}_2$   $\text{RO}_2+\text{HO}_2$  contributed ~80 %. As the rate coefficients are not well known and we cannot verify the modelling  
362 results for  $\text{HO}_2$  and  $\text{RO}_2$  our calculations serve solely as an indication of expected trends in the chemical system.

#### 363 4.1 Impact on overall HOM-formation

364 The top panel of **Fig. 2** shows the timeseries of  $\text{HOM-Mon}$  and  $\text{HOM-Acc}$  products. The  $\text{HOM-Mon}$  signal recovers after  
365 the oxidant adjustment, while the  $\text{HOM-Acc}$  signal is significantly suppressed at high  $\text{HO}_2/\text{RO}_2$ . This indicates that the shift  
366 from low to high  $\text{HO}_2/\text{RO}_2$  substantially impacts the termination reactions, shifting formation from the  $\text{HOM-Acc}$  product  
367 channel ( $\text{RO}_2+\text{RO}_2$ ) to the  $\text{HOM-Mon}$  channel.

368 An overview of the results for the product classes defined in the method section is shown in **Fig. 4**. Plotted are the average  
369 ratios of signal in the  $\text{NO}_3\text{-CIMS}$  in the high  $\text{HO}_2/\text{RO}_2$  steady state compared to the low  $\text{HO}_2/\text{RO}_2$  steady state. For better  
370 comparison, all experiment phases were normalized to the actual  $\alpha$ -pinene  $\text{OH}$  turnover. The overall  $\text{HOM}$ -signal was lower  
371 at high  $\text{HO}_2/\text{RO}_2$  showing a reduction of about 20 %. Most distinctive, the  $\text{HOM-Acc}$  were strongly reduced by about 60 %.  
372 A reduction of  $\text{HOM-Acc}$  by addition of  $\text{CO}$  was observed before by McFiggans et al. (2019), however there the  $\text{OH}$   
373 concentration was not kept constant. The  $\text{HOM-Frag}$  ( $5 \leq \text{C} < 10$ ) also show a reduction of about 20 %. At high  $\text{HO}_2/\text{RO}_2$   
374  $\text{C}_{10}\text{-HOM-RO}_2$  were also reduced significantly by about 40 %.

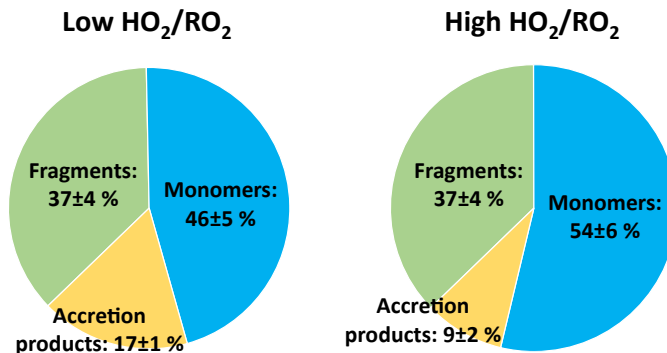


375

376 **Figure 4: Overview of average, relative change in product classes detected in  $\text{NO}_3\text{-CIMS}$  between low and high  $\text{HO}_2/\text{RO}_2$  case**  
377 **(both normalized to  $\alpha$ -pinene  $\text{OH}$  turnover) for unseeded experiments. Bars represent average of the two experiments, markers**  
378 **represent individual experiments.**

379 The  $\text{HOM-Mon}$  signal level remained about the same at low and high  $\text{HO}_2/\text{RO}_2$ . Without changes in the rates and  
380 contributions of the different termination reactions, the observed reduction in the  $\text{HOM-RO}_2$  precursors should lead to nearly  
381 the same reduction in  $\text{HOM-Mon}$ . However, the decrease of accretion product formation and fragmentation should lead to an  
382 increase in  $\text{HOM-Mon}$ . The presence of  $\text{HO}_2$  could reduce the alkoxy formation, and thus fragmentation of  $\text{HOM-RO}_2$ . This

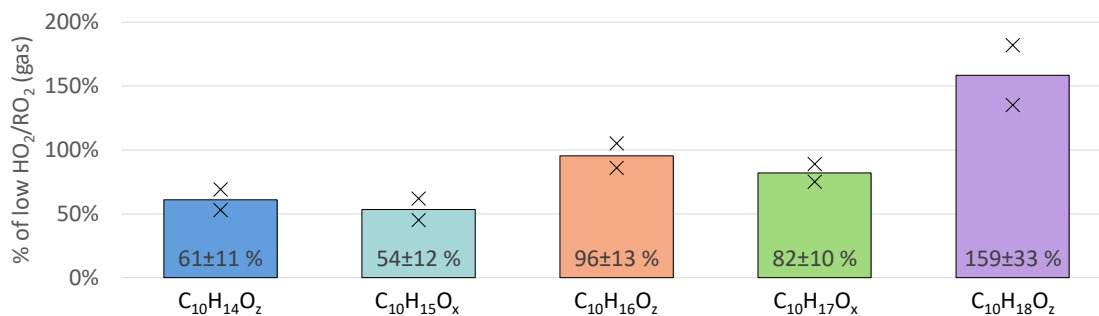
383 missing sink could lead to an additional HOM-Mon source compared to the low HO<sub>2</sub>/RO<sub>2</sub> case. However, the distribution of  
 384 the product classes at low and high HO<sub>2</sub>/RO<sub>2</sub> (**Fig. 5**) shows that contributions are shifted from HOM-Acc to HOM-Mon,  
 385 while the contribution of HOM-Frag remains constant. Each HOM-Acc is formed from one HOM-RO<sub>2</sub> (HOM-RO<sub>2</sub>+RO<sub>2</sub>) or  
 386 potentially even two HOM-RO<sub>2</sub> (HOM-RO<sub>2</sub>+HOM-RO<sub>2</sub>) and therefore each HOM-Acc not formed will lead to at least one  
 387 HOM-Mon.



388

389 **Figure 5: Average contribution of the closed shell product classes to overall HOM-product signal in the low and high HO<sub>2</sub>/RO<sub>2</sub>**  
 390 **cases (unseeded experiments).**

391 Further changes in the product distribution become evident when considering the individual HOM-Mon families as shown in  
 392 **Fig. 6**. The C<sub>10</sub>H<sub>15</sub>O<sub>x</sub> peroxy radical family and the related C<sub>10</sub>H<sub>14</sub>O<sub>z</sub> family (carbonyl compounds) show the strongest  
 393 suppression with a decrease of about 40 % at high HO<sub>2</sub>/RO<sub>2</sub>. For the C<sub>10</sub>H<sub>17</sub>O<sub>x</sub> peroxy radical family the suppression was  
 394 less pronounced with a 18 % reduction. In contrast, the C<sub>10</sub>H<sub>16</sub>O<sub>z</sub> family remained about the same while the C<sub>10</sub>H<sub>18</sub>O<sub>z</sub> family  
 395 showed a strong increase at high HO<sub>2</sub>/RO<sub>2</sub>.



396

397 **Figure 6: Overview of average, relative change in monomer families detected in NO<sub>3</sub>-CIMS between low and high HO<sub>2</sub>/RO<sub>2</sub> case**  
 398 **(both normalized to  $\alpha$ -pinene OH turnover) for unseeded experiments. Bars represent average of the two experiments, markers**  
 399 **represent individual experiments.**

400 The suppression of C<sub>10</sub>-HOM-RO<sub>2</sub> of only about 40 % compared to the reduction of overall [RO<sub>2</sub>] by ~70 % in the model  
 401 calculations (for the modelled concentrations see supplement **Sect. S4**) shows that in many instances the autoxidation is too  
 402 efficient to be out-competed by the RO<sub>2</sub>+HO<sub>2</sub> termination reaction, which is several times faster than RO<sub>2</sub>+RO<sub>2</sub> reactions.



403 Furthermore, the signal weighted O/C ratio of the monomer class does not change between low and high HO<sub>2</sub>/RO<sub>2</sub> (0.70±  
404 0.01). If the HO<sub>2</sub> termination would interrupt the autoxidation chain, a lower oxidation level would be expected at high  
405 HO<sub>2</sub>/RO<sub>2</sub>. The unchanged oxidation level and the suppression of HOM-Acc, indicate that the average autoxidation rate must  
406 be faster than  $k_{RO_2HO_2} \cdot [HO_2]$ , while the average accretion rate for  $k_{HOM-RO_2+RO_2} \cdot [RO_2]$  must be slower. In conclusion, the  
407 change in HO<sub>2</sub>/RO<sub>2</sub> should essentially impact the distribution of the HOM-RO<sub>2</sub> termination products.

## 408 4.2 Impact on HOM-RO<sub>2</sub>

409 C<sub>10</sub>-HOM-RO<sub>2</sub> are key to understand the changes in the HOM product distribution. Therefore, we will first discuss the  
410 changes in the HOM-RO<sub>2</sub> and then the changes in the closed shell products.

411 The C<sub>10</sub> peroxy radical class consists of the C<sub>10</sub>H<sub>15</sub>O<sub>x</sub> and C<sub>10</sub>H<sub>17</sub>O<sub>x</sub> families which were reduced to 54 % and 82 %,  
412 respectively when comparing the high and low HO<sub>2</sub>/RO<sub>2</sub> cases (**Fig. 6**, light blue and green bars). The observed reduction in  
413 C<sub>10</sub>-HOM-RO<sub>2</sub> is significantly smaller than the overall RO<sub>2</sub> concentration reduction predicted by the MCM model results  
414 (reduction to ~30 %). In the following paragraphs, we present a plausibility consideration to assess if these observed changes  
415 are consistent with our expectations from modelling results and reaction rates.

416 The change in the steady state concentration of a compound is always defined by the changes in its sources and sinks. The  
417 source of a HOM-RO<sub>2</sub> is the intramolecular reaction of a precursor RO<sub>2</sub> and thus the HOM-RO<sub>2</sub>'s source is reduced if the  
418 steady state concentration of the precursor RO<sub>2</sub> is reduced. However, assuming the source term of the precursor RO<sub>2</sub> is the  
419 same in low and high HO<sub>2</sub>/RO<sub>2</sub> (due to the constant  $\alpha$ -pinene OH turnover) and the precursor RO<sub>2</sub>'s sink term is dominated  
420 by the fast autoxidation in both cases, then the RO<sub>2</sub>'s steady state concentration would not be significantly changed. This  
421 consideration is only applicable for RO<sub>2</sub> where autoxidation dominates the sink term at low and high HO<sub>2</sub>/RO<sub>2</sub>. However,  
422 the unchanged oxidation level of the HOM-Mon indicates that once the autoxidation is initiated it out-competes the possible  
423 termination reactions.

424 In this case, the change in steady state concentration of the HOM-RO<sub>2</sub> will be defined by the changes in the sink terms.  
425 Owing to the faster reaction of RO<sub>2</sub>+HO<sub>2</sub> compared to RO<sub>2</sub>+RO<sub>2</sub> the chemical sink for all RO<sub>2</sub> including HOM-RO<sub>2</sub> with  
426 slower autoxidation rates increased, which leads to a reduction in the steady state concentration of RO<sub>2</sub> in general, despite  
427 holding the primary RO<sub>2</sub> source term constant.

428 For steady state conditions, we can estimate the expected effect on the RO<sub>2</sub> ratio between high and low HO<sub>2</sub>/RO<sub>2</sub> conditions  
429 for those HOM-RO<sub>2</sub> with production directly linked to the primary production ( $k_{OH} \cdot [OH] \cdot [\alpha\text{-pinene}]$ ) with negligible further  
430 autoxidation. The necessary equations and assumptions can be found in supplement **Sect. S7**. We assume the same primary  
431 production at low and high HO<sub>2</sub>/RO<sub>2</sub> and that the reaction with HO<sub>2</sub>, the reaction with RO<sub>2</sub> and the wall loss are the only  
432 significant loss pathways. At high HO<sub>2</sub>/RO<sub>2</sub>, a reduction to 80 % is expected if the chosen bulk rate constants are used  
433 ( $k_{RO_2HO_2}=2.46 \cdot 10^{-11} \text{ cm}^3 \cdot \text{s}^{-1}$  at 20 °C (Jenkin et al., 1997; Saunders et al., 2003),  $k_{RO_2RO_2}=5.0 \cdot 10^{-12} \text{ cm}^3 \cdot \text{s}^{-1}$ ). A reduction to

434 60 % is expected if  $k_{\text{RO}_2\text{HO}_2}$  is around 7 times faster than  $k_{\text{RO}_2\text{RO}_2}$  ( $k_{\text{RO}_2\text{RO}_2}=3.3\cdot 10^{-12} \text{ cm}^3\cdot\text{s}^{-1}$ ). These reductions are in the range  
435 of what is observed for the  $\text{C}_{10}\text{-HOM-RO}_2$ . Of course, the approach of using generalized bulk rate constants is limited, but  
436 the resulting values for  $k_{\text{RO}_2\text{RO}_2}$  were clearly within the range of rate coefficients expected for  $\text{HOM-RO}_2+\text{RO}_2$  reactions  
437 (Roldin et al., 2019) showing that the increased chemical sink is a plausible explanation for our observations.

438 The  $\text{C}_{10}\text{H}_{15}\text{O}_x$  family is on average reduced by around 30 % more than the  $\text{C}_{10}\text{H}_{17}\text{O}_x$  family (see **Fig. 6**).  $\text{C}_{10}\text{H}_{15}\text{O}_x$  peroxy  
439 radicals are either formed by sequential oxidation of  $\alpha$ -pinene, e.g. from oxidation products like pinonaldehyde, or directly  
440 from  $\alpha$ -pinene via the H-abstraction pathway (Shen et al., 2022). Formation of pinonaldehyde and, even more so HOM  
441 formation via the H-abstraction channel, involve alkoxy steps. However, alkoxy radicals should be reduced at high  $\text{HO}_2/\text{RO}_2$   
442 since they are mainly formed by  $\text{RO}_2+\text{RO}_2$  reactions in the absence of  $\text{NO}_x$ . Thus, missing source terms add to the increased  
443 chemical sink by  $\text{HO}_2$  for  $\text{C}_{10}\text{H}_{15}\text{O}_x$  peroxy radicals.

444 Amine CIMS measurements enabled detection of the formula composition  $\text{C}_{10}\text{H}_{16}\text{O}_2$  (e.g. pinonaldehyde).  $\text{C}_{10}\text{H}_{16}\text{O}_2$  was  
445 reduced on average to  $70\% \pm 1\%$  at high  $\text{HO}_2/\text{RO}_2$  compared to low  $\text{HO}_2/\text{RO}_2$ . This supports that a fraction of the  $\text{C}_{10}\text{H}_{15}\text{O}_x$   
446 radical decrease at high  $\text{HO}_2/\text{RO}_2$  arose from suppression of  $\text{C}_{10}\text{H}_{16}\text{O}_2$  first generation products. In addition, a further  
447 suppression of HOM formation via the H-abstraction channel is likely. It should be noted that the reduction of  $\text{C}_{10}\text{H}_{16}\text{O}_2$  is  
448 smaller than that expected by the MCM model results. Modelling results can be found in supplement **Sect. S4**. This might  
449 indicate that  $\text{HO}_2$  can also enable alkoxy radical steps to a certain degree as summarized by Jenkin et al. (2019) and  
450 postulated by e.g. Eddingsaas et al. (2012) as a source of pinonaldehyde in  $\text{HO}_2$  dominated systems.

451 According to the model calculations the pseudo first order rate coefficient  $k_{\text{RO}_2\text{HO}_2}\cdot[\text{HO}_2]$  is expected to be about  $0.04 \text{ s}^{-1}$  for  
452 the  $\text{RO}_2+\text{HO}_2$  reaction at high  $\text{HO}_2/\text{RO}_2$ . Consequently, only such  $\text{HOM-RO}_2$  with autoxidation rates of  $\leq 0.04 \text{ s}^{-1}$  will be  
453 significantly lost by reaction with  $\text{HO}_2$  at the higher  $\text{HO}_2$  concentrations. However, typical isomerization rates of peroxy  
454 radicals in autoxidation are of the order of  $0.1 \text{ s}^{-1}$  and many are faster (Piletic and Kleindienst, 2022; Berndt, 2021).  
455 Therefore, reduction in a  $\text{HOM-RO}_2$  is only expected when the faster termination rate of  $k_{\text{RO}_2\text{HO}_2}\cdot[\text{HO}_2]$  can compete with the  
456 autoxidation rate, i. e. when the autoxidation slows as the degree of oxidation increases on the specific  $\text{HOM-RO}_2$ . This  
457 consideration shows that the smaller reduction in  $\text{HOM-RO}_2$  compared to the lower oxidized  $\text{RO}_2$  in the model is compatible  
458 with fast autoxidation reactions that are missing in the MCM.

459 The increase in chemical sink strength by going from  $\text{RO}_2$  termination to  $\text{HO}_2$  termination is the main expected reason for  
460 the decrease in  $\text{C}_{10}\text{H}_{17}\text{O}_x$ . As discussed, the  $\text{C}_{10}\text{H}_{15}\text{O}_x$  family is subject to an additional decrease in the precursors due to the  
461 alkoxy steps necessary in the formation pathway. Since  $\text{C}_{10}\text{H}_{15}\text{O}_x$  were the main contributors to the  $\text{C}_{10}\text{-HOM-RO}_2$  class  
462 their stronger reduction is reflected in the overall reduction of  $\text{C}_{10}\text{-HOM-RO}_2$ .

#### 463 4.2.1 Contribution of C<sub>10</sub>H<sub>15</sub>O<sub>x</sub> and C<sub>10</sub>H<sub>17</sub>O<sub>x</sub> families to HOM-RO<sub>2</sub>

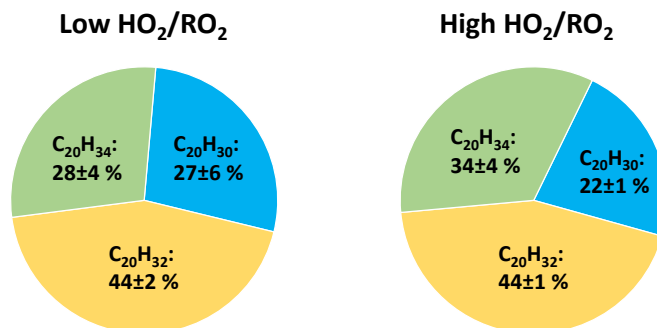
464 In the unseeded, pure gas phase experiments, the contribution of the C<sub>10</sub>H<sub>17</sub>O<sub>x</sub> family to the C<sub>10</sub>-HOM-RO<sub>2</sub> class is 23 %  
465 ±2 % on average in the low HO<sub>2</sub>/RO<sub>2</sub> case. In the high HO<sub>2</sub>/RO<sub>2</sub> case the contribution increases to 31 % ±4 % on average.  
466 As discussed above the suggested pathways to C<sub>10</sub>H<sub>15</sub>O<sub>x</sub> HOM-RO<sub>2</sub> may be additionally suppressed due to a decrease of  
467 alkoxy steps at high HO<sub>2</sub>/RO<sub>2</sub> reducing the entry channel into C<sub>10</sub>H<sub>15</sub>O<sub>x</sub> HOM-RO<sub>2</sub>.

468 Nevertheless, the contribution of C<sub>10</sub>H<sub>15</sub>O<sub>x</sub> is substantial in both experiment stages. Kang (2021) and Shen et al. (2022)  
469 reported that, in the photooxidation of α-pinene, the HOM-RO<sub>2</sub> detected by NO<sub>3</sub>-CIMS are dominated by the C<sub>10</sub>H<sub>15</sub>O<sub>x</sub>  
470 family, while C<sub>10</sub>H<sub>17</sub>O<sub>x</sub> formation is the main expected OH reaction pathway described in literature (Berndt, 2021; Berndt et  
471 al., 2016; Xu et al., 2019).

472 This hints towards an effective pathway to HOM via C<sub>10</sub>H<sub>15</sub>O<sub>x</sub>. A reason may be the fast opening of both carbon-rings in the  
473 bicyclic α-pinene (Shen et al., 2022), or a four-ring opening in pinonaldehyde or similar compounds, for easy autoxidation.  
474 From our observations increasing the HO<sub>2</sub>/RO<sub>2</sub> ratio does increase the relative importance of the C<sub>10</sub>H<sub>17</sub>O<sub>x</sub> family, but the  
475 change is less than 10 % in contribution.

476 Contribution of the two peroxy radical families to the HOM formation is also reflected in the composition of C<sub>20</sub> HOM-Acc.  
477 **Figure 7** shows the average contributions of the C<sub>20</sub>H<sub>30</sub>O<sub>z</sub>, C<sub>20</sub>H<sub>32</sub>O<sub>z</sub>, and C<sub>20</sub>H<sub>34</sub>O<sub>z</sub> families in the low and high HO<sub>2</sub>/RO<sub>2</sub>  
478 cases. Although the absolute amount of HOM-Acc was suppressed by 60 % the family distribution was similar, C<sub>20</sub>H<sub>32</sub>O<sub>z</sub>  
479 dominated, while C<sub>20</sub>H<sub>30</sub>O<sub>z</sub> was lowest. C<sub>20</sub>H<sub>30</sub>O<sub>z</sub> is formed from two members of the C<sub>10</sub>H<sub>15</sub>O<sub>x</sub> family, while C<sub>20</sub>H<sub>34</sub>O<sub>z</sub> is  
480 formed by two members of the C<sub>10</sub>H<sub>17</sub>O<sub>x</sub> family. C<sub>20</sub>H<sub>32</sub>O<sub>z</sub> is then a combination of a C<sub>10</sub>H<sub>15</sub>O<sub>x</sub>-RO<sub>2</sub> and C<sub>10</sub>H<sub>17</sub>O<sub>x</sub>-RO<sub>2</sub>.

481 Families that require one or two C<sub>10</sub>H<sub>17</sub>O<sub>x</sub> peroxy radicals for their formation have a higher contribution than the C<sub>10</sub>H<sub>17</sub>O<sub>x</sub>  
482 family's contribution to C<sub>10</sub>-HOM-RO<sub>2</sub>. Here, it is important to note that not only HOM-RO<sub>2</sub> can participate in HOM-Acc  
483 formation, but also traditional, less oxidized RO<sub>2</sub> radicals (Berndt et al., 2018; Pullinen et al., 2020; McFiggans et al., 2019),  
484 which are not detectable by NO<sub>3</sub><sup>-</sup>-CIMS. However, more oxidized peroxy radicals exhibit faster accretion rates (Berndt et al.,  
485 2018).



486

487 **Figure 7: Average contribution of the  $C_{20}H_{30}O_z$ ,  $C_{20}H_{32}O_z$ , and  $C_{20}H_{34}O_z$  family to the  $C_{20}$  HOM-Acc group signal in the low and**  
488 **high  $HO_2/RO_2$  cases (unseeded experiments). Not pictured is  $C_{20}H_{28}O_z$  due to its negligible signal (contribution  $\sim 1\%$ ).**

489 The large contributions of  $C_{20}H_{32}O_z$  and  $C_{20}H_{34}O_z$  thus clearly show the general importance of the  $C_{10}H_{17}O_x$  peroxy radicals.  
490 The largest fraction, the  $C_{20}H_{32}O_z$  family indicates the importance of HOM- $C_{10}H_{15}O_x$  and a high abundance of lower  
491 oxidized  $C_{10}H_{17}O_x$  peroxy radicals. Lower oxidized  $C_{10}H_{17}O_x-RO_2$  were recently measured by Berndt (2021). The fraction  
492 of  $C_{20}H_{34}O_z$  is smaller because their formation requires HOM- $C_{10}H_{17}O_x$  radicals which are less abundant compared to  
493 HOM- $C_{10}H_{15}O_x$ , while the small fraction of  $C_{20}H_{30}O_z$  indicates that, despite the importance of HOM- $C_{10}H_{15}O_x$ , lower  
494 oxidized  $C_{10}H_{15}O_x$  are less important.

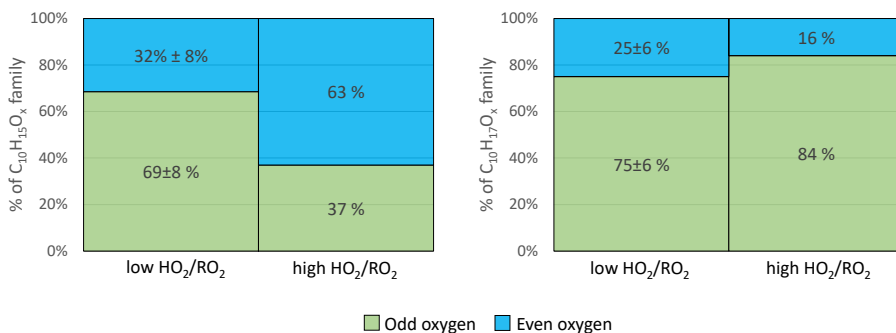
495 These results indicate the importance of mixed HOM-Acc formation by cross reactions of HOM- $RO_2$  and a lower oxidized  
496  $RO_2$ . The importance of mixed HOM-Acc is supported by the relatively small fractions of HOM-Acc products with very  
497 high oxygen numbers, which more likely stem from HOM- $RO_2$ +HOM- $RO_2$ . For example,  $C_{20}$ -HOM-Acc with 12 or more  
498 oxygen atoms contribute only around 30 % (low  $HO_2/RO_2$ : 26 %  $\pm 4\%$ , high  $HO_2/RO_2$ : 31 %  $\pm 2\%$ ) of the signal in the  
499 product group.

500 Although the effect of the changed  $HO_2/RO_2$  ratio is small, a tendency to higher  $C_{20}H_{34}O_z$  contribution was observed. This is  
501 consistent with the observation of a slightly higher  $C_{10}H_{17}O_x$  contribution to the  $C_{10}$ -HOM  $RO_2$ . The stronger suppression of  
502 the  $C_{10}H_{15}O_x$  family at high  $HO_2/RO_2$  is the first indication for, and can be explained by, a reduction in the alkoxy radical  
503 formation.

#### 504 4.2.2 Impact on HOM-Alkoxy radical formation

505 Alkoxy radicals (RO) are the second important radical type in the oxidation chain of  $\alpha$ -pinene. RO cannot be detected  
506 directly as they are highly unstable and thus have very low concentrations. However, as explained in **Sect. 2.1** the parity  
507 change in the HOM- $RO_2$  families can be used as a diagnosis tool for the abundance of alkoxy steps (Kang, 2021). A second  
508 indicator for alkoxy steps is the abundance of HOM products with less than 10 C-atoms.

509 **Figure 8** shows the average contribution of  $C_{10}H_{15}O_x$  and  $C_{10}H_{17}O_x$  with an even and odd number of oxygens at low and  
510 high  $HO_2/RO_2$ .  $C_{10}H_{15}O_x$  radicals with an even number of oxygens contribute on average 32 % at low  $HO_2/RO_2$ . For  
511  $C_{10}H_{15}O_x$ , the autoxidation chain is expected to start from an even number of oxygen either from  $C_{10}H_{15}O_4$  (pinonaldehyde-  
512 like) (MCM v3.3.1 (Jenkin et al., 1997; Saunders et al., 2003) or from  $C_{10}H_{15}O_2$  ( $C_{10}H_{16}$  H-abstraction) (Berndt, 2021; Shen  
513 et al., 2022). Therefore, without the involvement of an alkoxy step, the parity of the oxygen number in the observed  
514  $C_{10}H_{15}O_x$  HOM- $RO_2$  is expected to be even. Due to the average contribution of  $C_{10}H_{15}O_{\text{odd}}$  of 69 % we conclude that at least  
515 one alkoxy step (or any odd number of alkoxy steps) must have taken place in most of the cases at low  $HO_2/RO_2$ .



516

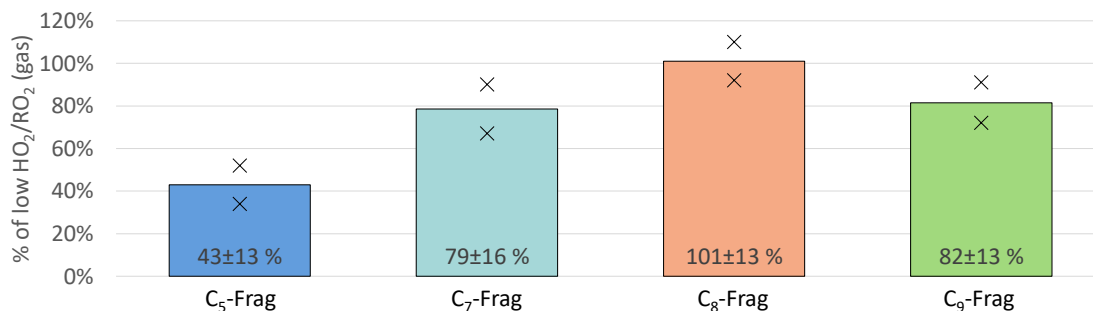
517 **Figure 8: Average contribution of  $O_{\text{odd}}$  and  $O_{\text{even}}$  to the HOM-RO<sub>2</sub> families  $C_{10}H_{15}O_x$  (left) and  $C_{10}H_{17}O_x$  (right) signal in the low**  
 518 **and high  $HO_2/RO_2$  cases (unseeded experiments).**

519 At high  $HO_2/RO_2$   $C_{10}H_{15}O_{\text{even}}$  contributed 63 % and the  $C_{10}H_{15}O_{\text{odd}}$  contribution was reduced to 37 %. This demonstrates a  
 520 change in the number of alkoxy steps along the formation pathway of the observed HOM-RO<sub>2</sub> radicals. The increased  
 521 contribution of  $C_{10}H_{15}O_{\text{even}}$  at high  $HO_2/RO_2$  lets us infer an even number of alkoxy steps as more common (0,2,4...). In the  
 522 simplest case 1 alkoxy step takes place at low  $HO_2/RO_2$  due to HOM-RO formation from HOM-RO<sub>2</sub>+RO<sub>2</sub> reactions, while  
 523 no alkoxy step takes place at high  $HO_2/RO_2$ , because HOM-RO<sub>2</sub>+HO<sub>2</sub> produces none or less HOM-RO than  
 524 HOM-RO<sub>2</sub>+RO<sub>2</sub>.

525 For  $C_{10}H_{17}O_x$  the entry channel into autoxidation is  $C_{10}H_{17}O_3$  with an odd number of oxygen atoms. Therefore, in  
 526 autoxidation without alkoxy steps the oxygen parity is expected to be odd. At low  $HO_2/RO_2$   $C_{10}H_{17}O_{\text{odd}}$  species contribute  
 527 75 % to the total  $C_{10}H_{17}O_x$  signal indicating that either none or an even number (2,4,...) of alkoxy steps occurred. At high  
 528  $HO_2/RO_2$  the odd contribution increases to 84 % (see **Fig. 8**). This result could indicate a low occurrence of alkoxy steps  
 529 even at low  $HO_2/RO_2$ , with a further decrease of alkoxy formation at high  $HO_2/RO_2$ . However, the observed shift is minor.

530 In any case the different responses of the  $C_{10}H_{15}O_x$  and  $C_{10}H_{17}O_x$  families to the reduction of HOM-RO<sub>2</sub> formation from  
 531 HOM-RO<sub>2</sub>+RO<sub>2</sub> at high  $HO_2/RO_2$  indicate that there could be fundamental differences in the autoxidation chains of  
 532  $C_{10}H_{15}O_x$  and  $C_{10}H_{17}O_x$  (or the limit of the parity analysis). The parity analysis indicates a decrease in alkoxy steps at high  
 533  $HO_2/RO_2$ , but it cannot be directly inferred with certainty. However, decrease in alkoxy steps at high  $HO_2/RO_2$  is supported  
 534 by the observation of changes in HOM-Frag products.

535 On average the sum of all HOM-Frag products (detected compounds with  $5 \leq C < 10$  by  $NO_3^-$ -CIMS) showed a reduction of  
 536 around 20 % (unseeded experiments, see **Fig. 4**). Further trends become recognizable when separating the species according  
 537 to their carbon number. **Figure 9** shows the  $C_5$ ,  $C_7$ ,  $C_8$ , and  $C_9$  HOM-Frag at high  $HO_2/RO_2$  compared to the low  $HO_2/RO_2$   
 538 case, normalized to the  $\alpha$ -pinene OH turnover. The fragment group with  $C_6$  compounds is not included, as it contributed less  
 539 than 5 % of the fragment signal and contained few detected compounds.



540

541 **Figure 9: Overview of average, relative change in C<sub>5</sub>, C<sub>7</sub>, C<sub>8</sub>, C<sub>9</sub> fragment groups detected in NO<sub>3</sub>-CIMS between high and low**  
 542 **HO<sub>2</sub>/RO<sub>2</sub> case (both normalized to  $\alpha$ -pinene OH turnover) for unseeded experiments. Bars represent average of the two**  
 543 **experiments, markers represent individual experiments.**

544 **Figure 9** shows a significant reduction in HOM-Frag with shorter carbon chain length: C<sub>5</sub> HOM-Frag are reduced by around  
 545 60 % compared to the low HO<sub>2</sub>/RO<sub>2</sub> case. If we assume that the fragmentation of C<sub>10</sub> compounds happens in consecutive  
 546 steps via scission of HOM-RO radicals (analogously to the MCM), this observation is in accord with decreasing importance  
 547 of alkoxy radical formation at high HO<sub>2</sub>/RO<sub>2</sub>.

548 Overall, all observations indicate strong involvement of RO in HOM formation as well as a reduced, but still significant,  
 549 involvement of RO at high HO<sub>2</sub>/RO<sub>2</sub>, when HO<sub>2</sub> chemistry dominates: This is supported by the change of the oxygen parity  
 550 in C<sub>10</sub>-HOM-RO<sub>2</sub>, and the decrease of fragmentation products, especially with lower carbon number, as well as the only  
 551 moderate reduction in the observed C<sub>10</sub>H<sub>16</sub>O<sub>2</sub> product (pinonaldehyde) and the still substantial importance of the C<sub>10</sub>H<sub>15</sub>O<sub>x</sub>  
 552 HOM-RO<sub>2</sub> family at high HO<sub>2</sub>/RO<sub>2</sub>.

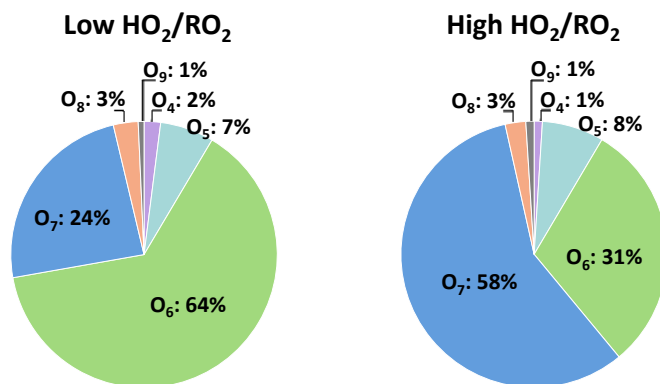
### 553 4.3 Impact on carbonyl and hydroperoxide formation

554 Increased HO<sub>2</sub>/RO<sub>2</sub> should shift the product distribution by reduction of alcohol and carbonyl compounds from the so-called  
 555 molecular channel in the RO<sub>2</sub>+RO<sub>2</sub> reaction (see reaction (**R3**)), in favor of hydroperoxide formation from RO<sub>2</sub>+HO<sub>2</sub>  
 556 termination (reaction (**RI**)). This effect can be best observed in the C<sub>10</sub>H<sub>18</sub>O<sub>z</sub> family, which contains the hydroperoxide and  
 557 alcohol termination products arising from C<sub>10</sub>H<sub>17</sub>O<sub>x</sub>. C<sub>10</sub>H<sub>18</sub>O<sub>z</sub> significantly increased to on average 159 % (see **Fig. 6**). This  
 558 supports an increased hydroperoxide formation, however, with some uncertainty due to the alcohol termination products  
 559 from C<sub>10</sub>H<sub>17</sub>O<sub>x</sub> (by reaction with RO<sub>2</sub>). To elucidate this further the contribution of individual species to the C<sub>10</sub>H<sub>18</sub>O<sub>z</sub> family  
 560 was examined.

561 Formation of an alcohol via the molecular path (reaction (**R3**)) leads to the loss of one oxygen atom compared to the  
 562 precursor C<sub>10</sub>H<sub>17</sub>O<sub>x</sub> radical, while in the hydroperoxide formation (reaction (**RI**)) the oxygen number remains the same. The  
 563 most abundant member of the C<sub>10</sub>H<sub>17</sub>O<sub>x</sub> family was C<sub>10</sub>H<sub>17</sub>O<sub>7</sub> with a contribution of 72 % ± 6 % at low HO<sub>2</sub>/RO<sub>2</sub>, and a  
 564 contribution of 82 % ± 1 % at high HO<sub>2</sub>/RO<sub>2</sub>. C<sub>10</sub>H<sub>17</sub>O<sub>7</sub> terminates to C<sub>10</sub>H<sub>18</sub>O<sub>z</sub> products either as an alcohol with sum  
 565 formula C<sub>10</sub>H<sub>18</sub>O<sub>6</sub>, or as a hydroperoxide with sum formula C<sub>10</sub>H<sub>18</sub>O<sub>7</sub>. These products have additional sources from C<sub>10</sub>H<sub>17</sub>O<sub>6</sub>

566 and  $C_{10}H_{17}O_8$  but due to the dominant contribution of  $C_{10}H_{17}O_7$  to the  $C_{10}H_{17}O_x$  family we expect any other production  
567 channels to be of minor importance.

568 **Figure 10** shows the HOM product distribution within the  $C_{10}H_{18}O_z$  family at low and high  $HO_2/RO_2$ . The sum of the  $O_6$  and  
569  $O_7$  product did not change significantly in the two regimes (about 88 %), showing that these are the major products, and  
570 agreeing well with the observation of  $C_{10}H_{17}O_7$  being the major  $C_{10}H_{17}O_x$  HOM- $RO_2$ . At low  $HO_2/RO_2$  the  $O_6$  product has a  
571 larger contribution of  $64 \% \pm 8 \%$ , while at high  $HO_2/RO_2$  ~30 % of signal is shifted to the  $O_7$  product. This shows that the  
572 increase in the  $C_{10}H_{18}O_z$  is matched with an increase of hydroperoxide formation.

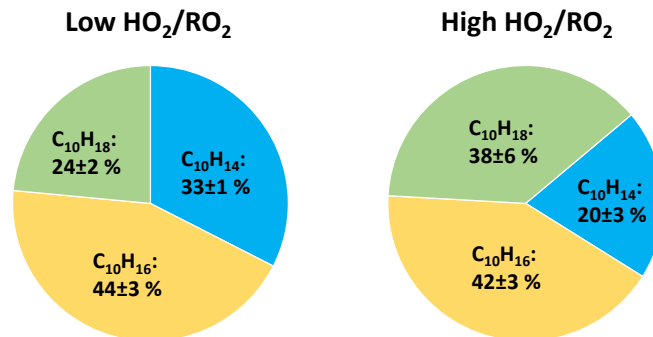


573

574 **Figure 10: Average contribution of the individual compounds to the  $C_{10}H_{18}O_z$  family signal at low and high  $HO_2/RO_2$  (unseeded  
575 experiments).**

576 An indicator for carbonyl formation is the  $C_{10}H_{14}O_z$  family as it only contains the carbonyl products arising from  
577  $C_{10}H_{15}O_x-RO_2$ . The  $C_{10}H_{14}O_z$  family was reduced on average to 61 % at high  $HO_2/RO_2$ , however this decrease matches the  
578 decrease in the  $C_{10}H_{15}O_x$  precursor family. If the reaction of a  $C_{10}H_{15}O_x$ -HOM- $RO_2$  with a second  $RO_2$  were the main  
579 formation pathway for  $C_{10}H_{14}O_z$  a stronger reduction would be expected as both precursor species were decreased  
580 significantly. Instead, it appears that  $C_{10}H_{14}O_z$  is mainly impacted by the decrease in  $C_{10}H_{15}O_x$  as their reductions are similar.  
581 A possible explanation could be that intramolecular termination is a major reaction pathway for  $C_{10}H_{15}O_x-RO_2$ , forming  
582  $C_{10}H_{14}O_x$ -carbonyls. Intramolecular termination of the autoxidation chain has been discussed in the literature for different  
583 VOCs (Shen et al., 2021; Guo et al., 2022), Rissanen et al. (2014) discussed the possible importance of the unimolecular  
584 termination via an H-shift, followed by formation of a carbonyl functional group and OH loss in the autoxidation chain of  
585 cyclohexene. Piletic and Kleindienst (2022) calculated fast reaction rate constants in the range of  $1-30 \text{ s}^{-1}$  for such  
586 intramolecular termination reactions to carbonyls for some  $C_{10}H_{17}O_5$  in the  $\alpha$ -pinene photooxidation, indicating that this  
587 pathway could also be significant for  $C_{10}H_{15}O_x$ . However, more investigation is necessary.

588 The overall contributions of the  $C_{10}H_{14}O_z$ ,  $C_{10}H_{16}O_z$ , and  $C_{10}H_{18}O_z$  families to the HOM-Mon class at high  $HO_2/RO_2$  are  
589 shifted as shown in **Fig. 11**.



590

591 **Figure 11: Average contribution of the  $C_{10}H_{14}O_z$ ,  $C_{10}H_{16}O_z$ , and  $C_{10}H_{18}O_z$  family to the monomer class signal at low and high**  
 592  **$HO_2/RO_2$  (unseeded experiments).**

593 The contribution of  $C_{10}H_{16}O_z$  is largest and remains similar in both cases, matching the already shown unchanged signal  
 594 level in **Fig. 6**. This is the case because the  $C_{10}H_{16}O_z$  family contains the alcohols from  $C_{10}H_{15}O_x+RO_2$ , carbonyls from  
 595  $C_{10}H_{17}O_x+RO_2$  and hydroperoxides from  $C_{10}H_{15}O_x+HO_2$  (see **Fig. 1**). A separation of the effects of enhanced  $HO_2$  on this  
 596 monomer family is difficult, as for the case where  $RO_2$  termination dominates vs. the case where  $HO_2$  termination dominates,  
 597 the loss of carbonyls and alcohols is partially compensated by the gain of hydroperoxides. A strong gain in hydroperoxides is  
 598 clearly reflected in the strong increase of  $C_{10}H_{18}O_z$  at high  $HO_2/RO_2$ .

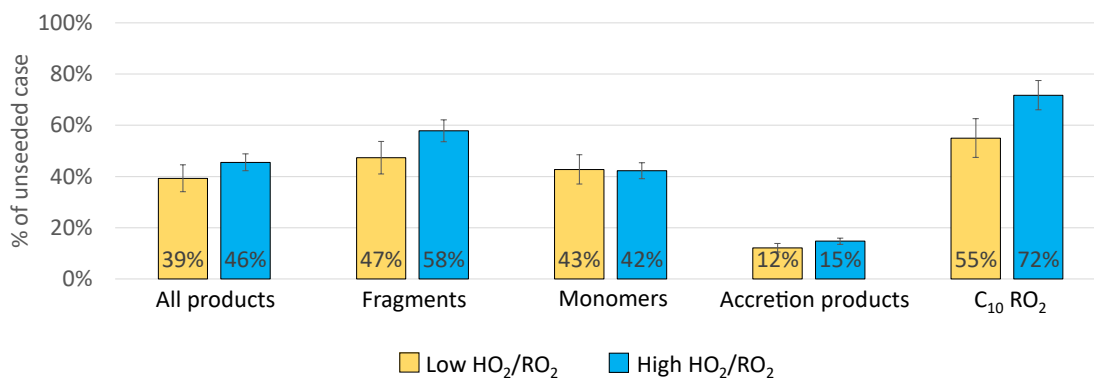
599 Inspection of the  $C_{10}H_{14}O_z$  and  $C_{10}H_{18}O_z$  families shows that ~13 % of the contribution by  $C_{10}H_{14}O_z$  are lost (carbonyls,  
 600 33 % at low  $HO_2/RO_2$ ) and are present instead as  $C_{10}H_{18}O_z$  (hydroperoxides), giving  $C_{10}H_{18}O_z$  a contribution of 38 % at high  
 601  $HO_2/RO_2$ .

#### 602 4.4 Impact on condensable organic mass

603 In the previous sections we demonstrated a shift of the product distribution by the shift from low to high  $HO_2/RO_2$   
 604 conditions. We also showed that the changes could be rationalized by generic mechanistic considerations. We added  
 605  $(NH_4)_2SO_4$  seed aerosol in two experiments to determine how the shift in the product distribution affects the condensable  
 606 organic mass by determining the fraction which remained in the gas-phase after seeding.

607 **Figure 12** shows the fraction remaining for the sum of all products as well as for the individual product classes for the high  
 608 and the low  $HO_2/RO_2$  case. In both cases a significant reduction of products in the gas phase was observed with seed present.  
 609 Overall, the sum of all products was reduced by around 60 %, with a slightly higher reduction in the low  $HO_2/RO_2$  case. This  
 610 can be attributed to the larger importance of HOM-Acc in the low  $HO_2/RO_2$  case, as well as to a 10 % lower reduction of the  
 611 HOM-Frag in the high  $HO_2/RO_2$  case. In both cases a reduction of the HOM- $RO_2$  is observed, which indicates that the  
 612 provided particle sink could have affected HOM formation chemistry, however only moderately.





613

614 **Figure 12: Overview of average, relative change in product classes signal between gas phase only and seeded system. Blue shows**  
 615 **the high HO<sub>2</sub>/RO<sub>2</sub> case, yellow the low HO<sub>2</sub>/RO<sub>2</sub> case. All are normalized to  $\alpha$ -pinene OH turnover, *Exp2* experiment. Error bars**  
 616 **represent result of error propagation (see supplement Sect. S9)**

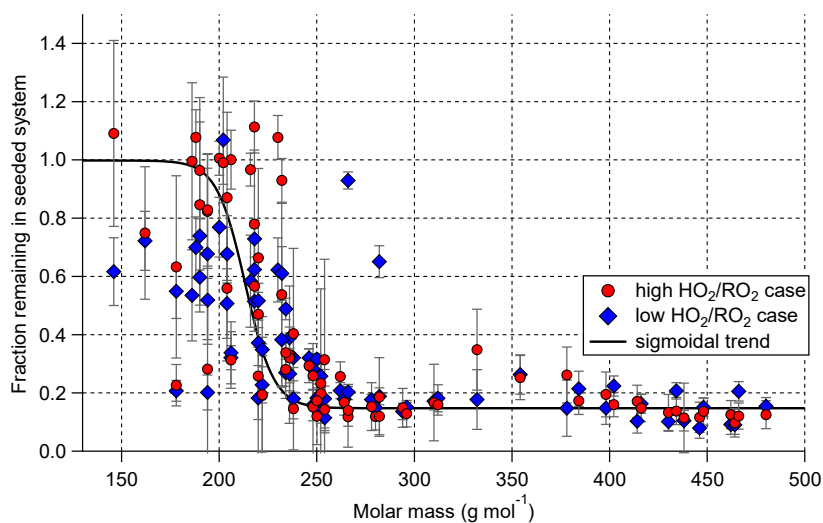
617 The total organic particulate mass was determined by AMS measurements and was 2.0  $\mu\text{g m}^{-3}$  and 3.4  $\mu\text{g m}^{-3}$  at high and low  
 618 HO<sub>2</sub>/RO<sub>2</sub> in the experiment (*Exp2*) displayed in **Fig. 12**. A reduction of condensed organic mass to 73 % $\pm$ 2 % at high  
 619 HO<sub>2</sub>/RO<sub>2</sub> (orange bar in **Fig. 14**) was observed on average. Since non-seeded and seeded experiments were conducted at  
 620 otherwise the same conditions and we did not observe significant new particle formation, the gas-phase compositions can be  
 621 directly compared. Therefore, we conclude that the shift in the product distribution led to a reduction of condensable material  
 622 at the same  $\alpha$ -pinene turnover with OH (and O<sub>3</sub>).

623 We calculated the wall loss corrected SOA yields with the corrected SOA mass as shown in **Eq. (4)** and as described by  
 624 Sarrafzadeh et al. (2016). To this end we used C<sub>10</sub>H<sub>16</sub>O<sub>7</sub> as the lead HOM compound. In the two experiments with seed  
 625 present (*Exp2.1* and *Exp3*) we had SOA yields of 7.3 % and 10.0 % at high HO<sub>2</sub>/RO<sub>2</sub> and 10.0 % and 12.8 % at low  
 626 HO<sub>2</sub>/RO<sub>2</sub>. The difference in the SOA yields between experiments can be explained by the slightly different OH  
 627 concentrations and subsequent difference in contribution by photooxidation (see **Table 1**). Overall, our yields are in the  
 628 lower range in comparison with the SOA yields reported by McFiggans et al. (2019) for the  $\alpha$ -pinene photooxidation.  
 629 However, our experiments were also performed at 5 °C higher temperature (20 °C) compared to 15 °C in McFiggans et al.  
 630 (2019)). The SOA yields show an absolute reduction of ~3 % at high HO<sub>2</sub>/RO<sub>2</sub> compared to low HO<sub>2</sub>/RO<sub>2</sub> (relative a  
 631 reduction of about 30 %). A reduction of the SOA yield of  $\alpha$ -pinene by addition of CO was described before by McFiggans  
 632 et al. (2019), however, there the  $\alpha$ -pinene OH turnover was not held constant.

633 The change from low to high HO<sub>2</sub>/RO<sub>2</sub> regime favored termination reactions to protic termination groups, as we observed  
 634 less carbonyl compounds and more hydroperoxides. This could overall shift the product distribution to products with lower  
 635 vapor pressures and favor SOA formation, since protic groups can act as hydrogen bond donors as well as hydrogen bond  
 636 acceptors. (As exemplified by the comparison of ethanol (boiling point (b.p) 78 °C) and ethane hydroperoxide (b.p. 93-  
 637 97 °C) with acetaldehyde (b.p. 20 °C) (Richter et al., 1955)). However, the effect of the termination group should be small  
 638 for HOM as they likely contain multiple hydroperoxide groups (compare Pullinen et al. (2020)). The reduction in HOM-Acc

639 is expected to decrease the condensable mass, since the HOM-Acc scavenge non-HOM-RO<sub>2</sub>, that would otherwise not  
640 partition into the particle phase.

641 Which of the measured compounds contribute significantly to the organic particle mass can be inferred by comparing their  
642 signal from the pure gas phase, unseeded cases to their signal with seed in the system. Under the assumptions that, for most  
643 HOM-compounds re-evaporation to the gas phase is negligible and that the precursor chemistry is not substantially disturbed  
644 by seed addition, the fraction of signal remaining with seed in the system reflects to which degree the compound is  
645 condensing. **Figure 13** shows the fraction remaining with seed in the system plotted against the molar mass of each  
646 individual compound. The plot includes all closed shell products that were measured with a relative standard deviation of  
647 less than 30 % for all measurement phases and depicts the results for both the high and low HO<sub>2</sub>/RO<sub>2</sub> case.



648

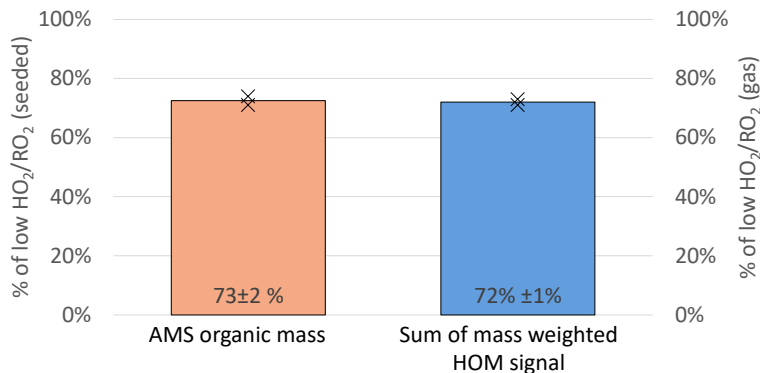
649 **Figure 13: Gas-phase fraction remaining in presence of seed (normalization of all data with  $\alpha$ -pinene OH turnover) for the low**  
650 **(blue) and high (red) HO<sub>2</sub>/RO<sub>2</sub> case. Displayed points represent all closed-shell compounds that were detected with relative**  
651 **standard deviation <30 % in all four experiment phases. Error bars represent result of error propagation (see supplement**  
652 **Sect. S9)**

653 Overall, in both cases we observed the same trend. Lighter compounds are not affected by the presence of seed particles, but  
654 with increasing molar mass the fraction remaining in the gas phase is reduced. A difference between the low and high  
655 HO<sub>2</sub>/RO<sub>2</sub> case can be observed in the low molar mass range: In the high HO<sub>2</sub>/RO<sub>2</sub> case many fragmentation products show a  
656 higher gas-phase fraction remaining up to 1. (In some cases, values larger than 1 were observed, however within the error  
657 limits. For the error estimation see supplement Sect. S9). Fractions remaining larger than 1 beyond error could be an  
658 indication that such products have a particle-phase production source. **Figure 13** also shows a critical SVOC/LVOC region  
659 for molar masses between 175 g mol<sup>-1</sup> and 250 g mol<sup>-1</sup> where neither a fraction remaining of 1 nor complete condensation is  
660 observed. The position of this region on the molar mass scale depends on the provided organic mass concentration. The large  
661 variation of the fraction remaining in this small range of molar masses shows that the partitioning coefficients are dependent

662 on the detailed structure of the compounds and not simply on their molar mass. The semi-volatile and low volatility products  
663 represent mainly higher oxidized fragments and HOM-Mon with less than 8 oxygen.

664 For compounds with a molar mass larger than  $250 \text{ g mol}^{-1}$  a constant fraction remaining is reached in steady state, which is  
665 due to an ongoing production of the compounds. From the condensation behavior shown in **Fig. 13** we conclude that the  
666 compounds heavier than  $230 \text{ g mol}^{-1}$  are expected to be of sufficiently low volatility to be mainly found in the particle phase  
667 for the organic mass present in the system and therefore contribute significantly to the SOA mass formation. Our finding  
668 agrees with the threshold used for low volatility HOM products in Pullinen et al. (2020).

669 Therefore, the signal of all compounds with a molar mass heavier than  $230 \text{ g mol}^{-1}$  was weighted with their molar mass and  
670 summed (see **Eq. (2)**). The ratio of this weighted signal sum at low and high  $\text{HO}_2/\text{RO}_2$  is then a measure of expected SOA  
671 mass loss. The calculation leads to an expected reduction to 72 % (blue bar, **Fig. 14**). This simplified approach leads to a  
672 good agreement with the AMS measurements and can thus explain the reduced particulate organic mass within the errors.



673

674 **Figure 14: Overview of the average, relative change in organic mass observed in the AMS (left y-axis, seeded experiments) and the**  
675 **mass weighted HOM signal observed in the  $\text{NO}_3$ -CIMS (right y-axis, unseeded experiments) between the low and high  $\text{HO}_2/\text{RO}_2$**   
676 **case (both normalized to  $\alpha$ -pinene OH turnover).**

677 To test for closure between HOM lost and particulate organic mass measured we approximated the upper limit of HOM  
678 concentration in the condensed phase. For this calculation we used the calibration factor determined for sulfuric acid for our  
679  $\text{NO}_3$ -MION-CIMS ( $7.0 \cdot 10^9 \text{ molecules} \cdot \text{cm}^{-3} \cdot \text{ncps}^{-1}$ ) and the relationship between gas and particulate concentration of a  
680 compound in the SAPHIR STAR chamber described in **Eq. (3)**. Again, we considered all compounds with  $M > 230 \text{ g mol}^{-1}$  in  
681 our calculation. The summed mass concentration lost from the gas phase was then compared to the SOA mass measured in  
682 the AMS. This comparison yields a good agreement within the uncertainties. The detailed calculation results can be found in  
683 the supplement (**Fig. S3**). Overall, an agreement within 40 % is achieved for all measurement stages.

684 The comparisons presented above show that we understand the processes governing the SOA formation in our chamber and  
685 that the NO<sub>3</sub>-CIMS measurements are well suited to observe the critical changes to understand the reduction in condensable  
686 organic material when shifting from low to high HO<sub>2</sub>/RO<sub>2</sub>.

## 687 **5 Conclusion**

688 In the presented series of experiments, we achieved a shift from a RO<sub>2</sub>+RO<sub>2</sub> dominated chemistry to a more atmospherically  
689 relevant HO<sub>2</sub>/RO<sub>2</sub> ratio under constant  $\alpha$ -pinene OH turnover. It was shown that moving towards atmospheric HO<sub>2</sub>/RO<sub>2</sub> ratio  
690 affected the SOA formation potential, with the observed organic mass being reduced at high HO<sub>2</sub>/RO<sub>2</sub>. This is in support of  
691 the potential bias towards high SOA yields in chamber studies at low HO<sub>2</sub>/RO<sub>2</sub> as discussed by Schervish and Donahue  
692 (2021). Our results confirm that too low HO<sub>2</sub>/RO<sub>2</sub> is one important parameter that can lead to an overestimated SOA yield in  
693 laboratory studies. In a broader picture the results show how important it is to consider the different contributions to the  
694 HOM-RO<sub>2</sub> sink (e.g. HO<sub>2</sub>, RO<sub>2</sub>, NO) when designing experiments and transferring laboratory results to the real atmosphere.

695 The gas-phase observations showed that the SOA reduction at high HO<sub>2</sub>/RO<sub>2</sub> was mainly due to a reduced HOM-Acc  
696 formation which were formed by RO<sub>2</sub>+RO<sub>2</sub> cross reactions in the low HO<sub>2</sub>/RO<sub>2</sub> cases. This prevented contribution to SOA  
697 by less oxidized RO<sub>2</sub> which were scavenged in the HOM-Acc at low HO<sub>2</sub>/RO<sub>2</sub>. Under atmospheric condition such cross  
698 reactions are less important, and such (mixed) accretion products would contribute less to SOA.

699 The overall observed HOM-products were reduced slightly, showing that under certain circumstances RO<sub>2</sub>+HO<sub>2</sub> termination  
700 can impede the HOM formation, mainly by reducing the precursor RO<sub>2</sub> levels and less by impeding the autoxidation itself.  
701 The autoxidation chain (once initiated) runs to a similar oxidation level at both high and low HO<sub>2</sub>/RO<sub>2</sub>. The observed  
702 HOM-Mon products shift significantly between monomer families due to the different termination reaction. A decrease in  
703 carbonyl and alcohol formation from RO<sub>2</sub>+RO<sub>2</sub> and an increase in hydroperoxide formation from RO<sub>2</sub>+HO<sub>2</sub> was observed at  
704 high HO<sub>2</sub>/RO<sub>2</sub>.

705 Furthermore, a reduction in HOM-Frag products, especially with lower carbon numbers, as well as the parity of the C<sub>10</sub>H<sub>15</sub>O<sub>x</sub>  
706 HOM-RO<sub>2</sub> show a reduction in alkoxy radical formation at high HO<sub>2</sub>/RO<sub>2</sub>. The moderate reduction in larger HOM-Frag  
707 products and pinonaldehyde, however, suggest that some alkoxy radical steps are still important. This raises the question of  
708 whether alkoxy radical formation can be facilitated by HO<sub>2</sub>. In the atmosphere such effects are most often overcome  
709 whenever RO<sub>2</sub>+NO is the major alkoxy radical source.

710 Overall, the observed changes in the gas phase could be well explained with the presented generic mechanistic understanding  
711 of HOM formation in the  $\alpha$ -pinene system. The addition of seed demonstrated that the shift towards high HO<sub>2</sub>/RO<sub>2</sub> reduced  
712 the condensable organic mass, stressing the importance of controlling higher order reactions of peroxy radicals which lead to  
713 overemphasis of HOM-Acc product formation at low HO<sub>2</sub>/RO<sub>2</sub> ratios.

714 Furthermore, the seed addition allowed us to determine which products were contributing to the SOA formation and show  
715 that their volatility is a function of molar mass and detailed molecular structure. This revealed a critical mass region in which  
716 compounds have significant fractions in gas and particulate phase. Based on absorptive partitioning theory the volatilities at  
717 which this critical region is found should depend on the organic mass present in the system.

718 Valuable insight about the condensed phase can be gained from HOM gas phase measurements. We inferred conclusions  
719 about the particulate phase from the gas phase measurements and compared them to the direct particle phase observations,  
720 finding good agreements between our expectations and the measurements.

#### 721 **Data availability**

722 Information about all steady-state conditions utilized, as well as the data necessary to reproduce the figures in this study are  
723 available at <https://doi.org/10.26165/JUELICH-DATA/R8ITFE>.

#### 724 **Author contribution**

725 TFM, MH and GM conceptualized the study and TFM, YB, SK and SRZ designed the experiments and developed the  
726 analysis methodology. The experiments were performed by YB, SK, VG and SRZ. Instrument deployment and/or data  
727 analysis were performed by YB, SK, HW, RW, JX, AZ, QH, TZ and VG. YB did model calculations of the experiments.  
728 AV, SPO, TJB, MG and MH provided counsel on experiment design and data interpretation. The compiled data set was  
729 interpreted by YB and TFM, and the results were discussed by all co-authors. YB visualized the data and YB and TFM  
730 prepared the manuscript. All co-authors reviewed the manuscript.

#### 731 **Competing interests**

732 The authors declare that they have no conflict of interest.

#### 733 **Financial support**

734 This research has received funding from the European Union's Horizon 2020 research and innovation programme under the  
735 FORCeS grant agreement No 821205, the Federal Ministry of Education and Research (BMBF) Germany under the FONA  
736 Strategy "Research for Sustainability" as part of the implementation of ACTRIS-D under the funding code 01LK200010,  
737 Vetenskapsrådet (VR, grant agreement No. 2018-04430), Svenska Forskningsrådet Formas (grant agreement No. 2019-586)  
738 and the Natural Environment Research Council (NERC) UK under the grant agreement No. NE/V012665/1.

739 **References**

- 740 Albrecht, S. R., Novelli, A., Hofzumahaus, A., Kang, S., Baker, Y., Mentel, T., Wahner, A., and Fuchs, H.: Measurements of  
741 hydroperoxy radicals (HO<sub>2</sub>) at atmospheric concentrations using bromide chemical ionisation mass spectrometry, *Atmos.*  
742 *Meas. Tech.*, 12, 891-902, <https://doi.org/10.5194/amt-12-891-2019>, 2019.
- 743 Atkinson, R. and Arey, J.: Atmospheric degradation of volatile organic compounds, *Chem. Rev.*, 103, 4605-4638,  
744 <https://doi.org/10.1021/cr0206420>, 2003.
- 745 Berndt, T.: Peroxy Radical Processes and Product Formation in the OH Radical-Initiated Oxidation of  $\alpha$ -Pinene for Near-  
746 Atmospheric Conditions, *J. Phys. Chem. A*, 125, 9151-9160, <https://doi.org/10.1021/acs.jpca.1c05576>, 2021.
- 747 Berndt, T., Mentler, B., Scholz, W., Fischer, L., Herrmann, H., Kulmala, M., and Hansel, A.: Accretion product formation  
748 from ozonolysis and OH radical reaction of  $\alpha$ -pinene: mechanistic insight and the influence of isoprene and ethylene,  
749 *Environ. Sci. Technol.*, 52, 11069-11077, <https://doi.org/10.1021/acs.est.8b02210>, 2018.
- 750 Berndt, T., Richters, S., Jokinen, T., Hyttinen, N., Kurtén, T., Otkjaer, R. V., Kjaergaard, H. G., Stratmann, F., Herrmann,  
751 H., Sipila, M., Kulmala, M., and Ehn, M.: Hydroxyl radical-induced formation of highly oxidized organic compounds, *Nat.*  
752 *Commun.*, 7, 13677, <https://doi.org/10.1038/ncomms13677>, 2016.
- 753 Bianchi, F., Garmash, O., He, X. C., Yan, C., Iyer, S., Rosendahl, I., Xu, Z. N., Rissanen, M. P., Riva, M., Taipale, R.,  
754 Sarnela, N., Petäjä, T., Worsnop, D. R., Kulmala, M., Ehn, M., and Junninen, H.: The role of highly oxygenated molecules  
755 (HOMs) in determining the composition of ambient ions in the boreal forest, *Atmos. Chem. Phys.*, 17, 13819-13831,  
756 <https://doi.org/10.5194/acp-17-13819-2017>, 2017.
- 757 Bianchi, F., Kurtén, T., Riva, M., Mohr, C., Rissanen, M. P., Roldin, P., Berndt, T., Crouse, J. D., Wennberg, P. O., Mentel,  
758 T. F., Wildt, J., Junninen, H., Jokinen, T., Kulmala, M., Worsnop, D. R., Thornton, J. A., Donahue, N., Kjaergaard, H. G.,  
759 and Ehn, M.: Highly Oxygenated Organic Molecules (HOM) from Gas-Phase Autoxidation Involving Peroxy Radicals: A  
760 Key Contributor to Atmospheric Aerosol, *Chem. Rev.*, 119, 3472-3509, <https://doi.org/10.1021/acs.chemrev.8b00395>, 2019.
- 761 Cox, R. A., Ammann, M., Crowley, J. N., Herrmann, H., Jenkin, M. E., McNeill, V. F., Mellouki, A., Troe, J., and  
762 Wallington, T. J.: Evaluated kinetic and photochemical data for atmospheric chemistry: Volume VII – Criegee intermediates,  
763 *Atmos. Chem. Phys.*, 20, 13497-13519, <https://doi.org/10.5194/acp-20-13497-2020>, 2020.
- 764 Crouse, J. D., Nielsen, L. B., Jørgensen, S., Kjaergaard, H. G., and Wennberg, P. O.: Autoxidation of organic compounds in  
765 the atmosphere, *J. Phys. Chem. Lett.*, 4, 3513-3520, <https://doi.org/10.1021/jz4019207>, 2013.
- 766 Docherty, K. S. and Ziemann, P. J.: Effects of stabilized criegee intermediate and OH radical scavengers on aerosol  
767 formation from reactions of  $\beta$ -pinene with O<sub>3</sub>, *Aerosol Sci. Tech.*, 37, 877-891, <https://doi.org/10.1080/02786820300930>,  
768 2003.
- 769 Eddingsaas, N., Loza, C., Yee, L., Seinfeld, J., and Wennberg, P.:  $\alpha$ -Pinene photooxidation under controlled chemical  
770 conditions – Part 1: Gas-phase composition in low- and high-NO<sub>x</sub> environments, *Atmos. Chem. Phys.*, 12, 6489-6504,  
771 <https://doi.org/10.5194/acp-12-6489-2012>, 2012.
- 772 Ehn, M., Thornton, J. A., Kleist, E., Sipila, M., Junninen, H., Pullinen, I., Springer, M., Rubach, F., Tillmann, R., Lee, B.,  
773 Lopez-Hilfiker, F., Andres, S., Acir, I. H., Rissanen, M., Jokinen, T., Schobesberger, S., Kangasluoma, J., Kontkanen, J.,  
774 Nieminen, T., Kurtén, T., Nielsen, L. B., Jørgensen, S., Kjaergaard, H. G., Canagaratna, M., Maso, M. D., Berndt, T., Petaja,  
775 T., Wahner, A., Kerminen, V. M., Kulmala, M., Worsnop, D. R., Wildt, J., and Mentel, T. F.: A large source of low-  
776 volatility secondary organic aerosol, *Nature*, 506, 476-479, <https://doi.org/10.1038/nature13032>, 2014.

777 Eisele, F. and Tanner, D.: Measurement of the gas phase concentration of H<sub>2</sub>SO<sub>4</sub> and methane sulfonic acid and estimates of  
778 H<sub>2</sub>SO<sub>4</sub> production and loss in the atmosphere, *J. Geophys. Res. Atmos.*, 98, 9001-9010, <https://doi.org/10.1029/93JD00031>,  
779 1993.

780 Fantechi, G., Vereecken, L., and Peeters, J.: The OH-initiated atmospheric oxidation of pinonaldehyde: Detailed theoretical  
781 study and mechanism construction, *Phys. Chem. Chem. Phys.*, 4, 5795-5805, <https://doi.org/10.1039/B205901K> 2002.

782 Guo, Y., Shen, H., Pullinen, I., Luo, H., Kang, S., Vereecken, L., Fuchs, H., Hallquist, M., Acir, I. H., Tillmann, R., Rohrer,  
783 F., Wildt, J., Kiendler-Scharr, A., Wahner, A., Zhao, D. F., and Mentel, T. F.: Identification of highly oxygenated organic  
784 molecules and their role in aerosol formation in the reaction of limonene with nitrate radical, *Atmos. Chem. Phys.*, 22,  
785 11323-11346, <https://doi.org/10.5194/acp-22-11323-2022>, 2022.

786 Hallquist, M., Wenger, J. C., Baltensperger, U., Rudich, Y., Simpson, D., Claeys, M., Dommen, J., Donahue, N. M., George,  
787 C., Goldstein, A. H., Hamilton, J. F., Herrmann, H., Hoffmann, T., Iinuma, Y., Jang, M., Jenkin, M. E., Jimenez, J. L.,  
788 Kiendler-Scharr, A., Maenhaut, W., McFiggans, G., Mentel, T. F., Monod, A., Prévôt, A. S. H., Seinfeld, J. H., Surratt, J. D.,  
789 Szmigielski, R., and Wildt, J.: The formation, properties and impact of secondary organic aerosol: current and emerging  
790 issues, *Atmos. Chem. Phys.*, 9, 5155-5236, <https://doi.org/10.5194/acp-9-5155-2009>, 2009.

791 Hantschke, L. L.: Oxidation of monoterpenes studied in atmospheric simulation chambers, Forschungszentrum Jülich  
792 GmbH, Zentralbibliothek, Verlag, 2022.

793 Hasson, A. S., Kuwata, K. T., Arroyo, M. C., and Petersen, E. B.: Theoretical studies of the reaction of hydroperoxy radicals  
794 (HO<sub>2</sub>) with ethyl peroxy (CH<sub>3</sub>CH<sub>2</sub>O<sub>2</sub>), acetyl peroxy (CH<sub>3</sub>C(O)O<sub>2</sub>), and acetonyl peroxy (CH<sub>3</sub>C(O)CH<sub>2</sub>O<sub>2</sub>) radicals, *J.*  
795 *Photochem. Photobiol. A*, 176, 218-230, <https://doi.org/10.1016/j.jphotochem.2005.08.012>, 2005.

796 Henry, K. M., Lohaus, T., and Donahue, N. M.: Organic aerosol yields from  $\alpha$ -pinene oxidation: bridging the gap between  
797 first-generation yields and aging chemistry, *Environ. Sci. Technol.*, 46, 12347-12354, <https://doi.org/10.1021/es302060y>,  
798 2012.

799 Hidy, G.: Atmospheric chemistry in a box or a bag, *Atmos.*, 10, 401, <https://doi.org/10.3390/atmos10070401>, 2019.

800 Hyttinen, N., Otkjær, R. V., Iyer, S., Kjaergaard, H. G., Rissanen, M. P., Wennberg, P. O., and Kurtén, T.: Computational  
801 comparison of different reagent ions in the chemical ionization of oxidized multifunctional compounds, *J. Phys. Chem. A*,  
802 122, 269-279, <https://doi.org/10.1021/acs.jpca.7b10015>, 2018.

803 Iyer, S., Reiman, H., Møller, K. H., Rissanen, M. P., Kjaergaard, H. G., and Kurtén, T.: Computational investigation of  
804 RO<sub>2</sub>+ HO<sub>2</sub> and RO<sub>2</sub>+ RO<sub>2</sub> reactions of monoterpene derived first-generation peroxy radicals leading to radical recycling, *J.*  
805 *Phys. Chem. A*, 122, 9542-9552, <https://doi.org/10.1021/acs.jpca.8b09241>, 2018.

806 Iyer, S., Rissanen, M. P., Valiev, R., Barua, S., Krechmer, J. E., Thornton, J., Ehn, M., and Kurtén, T.: Molecular mechanism  
807 for rapid autoxidation in  $\alpha$ -pinene ozonolysis, *Nat. Commun.*, 12, 878, <https://doi.org/10.1038/s41467-021-21172-w>, 2021.

808 Jenkin, M. E., Saunders, S. M., and Pilling, M. J.: The tropospheric degradation of volatile organic compounds: a protocol  
809 for mechanism development, *Atmos. Environ.*, 31, 81-104, [https://doi.org/10.1016/S1352-2310\(96\)00105-7](https://doi.org/10.1016/S1352-2310(96)00105-7), 1997.

810 Jenkin, M. E., Valorso, R., Aumont, B., and Rickard, A. R.: Estimation of rate coefficients and branching ratios for reactions  
811 of organic peroxy radicals for use in automated mechanism construction, *Atmos. Chem. Phys.*, 19, 7691-7717,  
812 <https://doi.org/10.5194/acp-19-7691-2019>, 2019.

- 813 Johnson, D. and Marston, G.: The gas-phase ozonolysis of unsaturated volatile organic compounds in the troposphere,  
814 Chem. Soc. Rev., 37, 699-716, <https://doi.org/10.1039/B704260B> 2008.
- 815 Junninen, H., Ehn, M., Petäjä, T., Luosujärvi, L., Kotiaho, T., Kostianen, R., Rohner, U., Gonin, M., Fuhrer, K., Kulmala,  
816 M., and Worsnop, D. R.: A high-resolution mass spectrometer to measure atmospheric ion composition, Atmos. Meas.  
817 Tech., 3, 1039-1053, <https://doi.org/10.5194/amt-3-1039-2010>, 2010.
- 818 Kang, S.: Formation of highly oxygenated organic molecules from  $\alpha$ -pinene photochemistry, Forschungszentrum Jülich  
819 GmbH, 2021.
- 820 Keywood, M., Kroll, J., Varutbangkul, V., Bahreini, R., Flagan, R., and Seinfeld, J.: Secondary organic aerosol formation  
821 from cyclohexene ozonolysis: Effect of OH scavenger and the role of radical chemistry, Environ. Sci. Technol., 38, 3343-  
822 3350, <https://doi.org/10.1021/es049725j>, 2004.
- 823 Khan, M., Cooke, M., Utembe, S., Archibald, A., Derwent, R., Jenkin, M. E., Morris, W., South, N., Hansen, J., Francisco,  
824 J., Percival, C. J., and Shallcross, D. E.: Global analysis of peroxy radicals and peroxy radical-water complexation using the  
825 STOCHEM-CRI global chemistry and transport model, Atmospheric Environment, 106, 278-287,  
826 <https://doi.org/10.1016/j.atmosenv.2015.02.020>, 2015.
- 827 Kiendler-Scharr, A., Wildt, J., Maso, M. D., Hohaus, T., Kleist, E., Mentel, T. F., Tillmann, R., Uerlings, R., Schurr, U., and  
828 Wahner, A.: New particle formation in forests inhibited by isoprene emissions, Nature, 461, 381-384,  
829 <https://doi.org/10.1038/nature08292>, 2009.
- 830 McFiggans, G., Mentel, T. F., Wildt, J., Pullinen, I., Kang, S., Kleist, E., Schmitt, S., Springer, M., Tillmann, R., Wu, C.,  
831 Zhao, D., Hallquist, M., Faxon, C., Le Breton, M., Hallquist, A. M., Simpson, D., Bergstrom, R., Jenkin, M. E., Ehn, M.,  
832 Thornton, J. A., Alfarra, M. R., Bannan, T. J., Percival, C. J., Priestley, M., Topping, D., and Kiendler-Scharr, A.: Secondary  
833 organic aerosol reduced by mixture of atmospheric vapours, Nature, 565, 587-593, <https://doi.org/10.1038/s41586-018-0871-y>, 2019.
- 835 Mentel, T., Springer, M., Ehn, M., Kleist, E., Pullinen, I., Kurtén, T., Rissanen, M., Wahner, A., and Wildt, J.: Formation of  
836 highly oxidized multifunctional compounds: autoxidation of peroxy radicals formed in the ozonolysis of alkenes—deduced  
837 from structure–product relationships, Atmos. Chem. Phys., 15, 6745-6765, <https://doi.org/10.5194/acp-15-6745-2015>, 2015.
- 838 Mentel, T. F., Wildt, J., Kiendler-Scharr, A., Kleist, E., Tillmann, R., Dal Maso, M., Fisseha, R., Hohaus, T., Spahn, H.,  
839 Uerlings, R., Wegener, R., Griffiths, P. T., Dinar, E., Rudich, Y., and Wahner, A.: Photochemical production of aerosols  
840 from real plant emissions, Atmos. Chem. Phys., 9, 4387-4406, <https://doi.org/10.5194/acp-9-4387-2009>, 2009.
- 841 Mohr, C., Thornton, J. A., Heitto, A., Lopez-Hilfiker, F. D., Lutz, A., Riipinen, I., Hong, J., Donahue, N. M., Hallquist, M.,  
842 Petaja, T., Kulmala, M., and Yli-Juuti, T.: Molecular identification of organic vapors driving atmospheric nanoparticle  
843 growth, Nat. Commun., 10, 4442, <https://doi.org/10.1038/s41467-019-12473-2>, 2019.
- 844 Otkjaer, R. V., Jakobsen, H. H., Tram, C. M., and Kjaergaard, H. G.: Calculated Hydrogen Shift Rate Constants in  
845 Substituted Alkyl Peroxy Radicals, J. Phys. Chem. A, 122, 8665-8673, <https://doi.org/10.1021/acs.jpca.8b06223>, 2018.
- 846 Piletic, I. R. and Kleindienst, T. E.: Rates and yields of unimolecular reactions producing highly oxidized peroxy radicals in  
847 the OH-induced autoxidation of  $\alpha$ -pinene,  $\beta$ -pinene, and limonene, J. Phys. Chem. A, 126, 88-100,  
848 <https://doi.org/10.1021/acs.jpca.1c07961>, 2022.
- 849 Pullinen, I., Schmitt, S., Kang, S., Sarrafzadeh, M., Schlag, P., Andres, S., Kleist, E., Mentel, T. F., Rohrer, F., Springer, M.,  
850 Tillmann, R., Wildt, J., Wu, C., Zhao, D., Wahner, A., and Kiendler-Scharr, A.: Impact of NO<sub>x</sub> on secondary organic aerosol



- 851 (SOA) formation from  $\alpha$ -pinene and  $\beta$ -pinene photooxidation: the role of highly oxygenated organic nitrates, *Atmos. Chem.*  
852 *Phys.*, 20, 10125-10147, <https://doi.org/10.5194/acp-20-10125-2020>, 2020.
- 853 Richter, F., Ostertag, R., Ammerlahn, G., Behrle, E., Baumann, M., and Kobel, M.: Beilstein's handbook of organic  
854 chemistry. Third supplement, covering the literature from 1930-1949, 1955.
- 855 Rissanen, M. P., Mikkilä, J., Iyer, S., and Hakala, J.: Multi-scheme chemical ionization inlet (MION) for fast switching of  
856 reagent ion chemistry in atmospheric pressure chemical ionization mass spectrometry (CIMS) applications, *Atmos. Meas.*  
857 *Tech.*, 12, 6635-6646, <https://doi.org/10.5194/amt-12-6635-2019>, 2019.
- 858 Rissanen, M. P., Kurtén, T., Sipila, M., Thornton, J. A., Kangasluoma, J., Sarnela, N., Junninen, H., Jorgensen, S.,  
859 Schallhart, S., Kajos, M. K., Taipale, R., Springer, M., Mentel, T. F., Ruuskanen, T., Petaja, T., Worsnop, D. R., Kjaergaard,  
860 H. G., and Ehn, M.: The formation of highly oxidized multifunctional products in the ozonolysis of cyclohexene, *J. Am.*  
861 *Chem. Soc.*, 136, 15596-15606, <https://doi.org/10.1021/ja507146s>, 2014.
- 862 Roldin, P., Ehn, M., Kurtén, T., Olenius, T., Rissanen, M. P., Sarnela, N., Elm, J., Rantala, P., Hao, L., Hyttinen, N.,  
863 Heikkinen, L., Worsnop, D. R., Pichelstorfer, L., Xavier, C., Clusius, P., Öström, E., Petäjä, T., Kulmala, M., Vehkamäki,  
864 H., Virtanen, A., Riipinen, I., and Boy, M.: The role of highly oxygenated organic molecules in the Boreal aerosol-cloud-  
865 climate system, *Nat. Commun.*, 10, 4370, <https://doi.org/10.1038/s41467-019-12338-8>, 2019.
- 866 Sanchez, J., Tanner, D. J., Chen, D., Huey, L. G., and Ng, N. L.: A new technique for the direct detection of HO<sub>2</sub> radicals  
867 using bromide chemical ionization mass spectrometry (Br-CIMS): initial characterization, *Atmos. Meas. Tech.*, 9, 3851-  
868 3861, <https://doi.org/10.5194/amt-9-3851-2016>, 2016.
- 869 Sarrafzadeh, M., Wildt, J., Pullinen, I., Springer, M., Kleist, E., Tillmann, R., Schmitt, S. H., Wu, C., Mentel, T. F., Zhao,  
870 D., Hastie, D. R., and Kiendler-Scharr, A.: Impact of NO<sub>x</sub> and OH on secondary organic aerosol formation from  $\beta$ -pinene  
871 photooxidation, *Atmos. Chem. Phys.*, 16, 11237-11248, <https://doi.org/10.5194/acp-16-11237-2016>, 2016.
- 872 Saunders, S. M., Jenkin, M. E., Derwent, R., and Pilling, M.: Protocol for the development of the Master Chemical  
873 Mechanism, MCM v3 (Part A): tropospheric degradation of non-aromatic volatile organic compounds, *Atmos. Chem. Phys.*,  
874 3, 161-180, <https://doi.org/10.5194/acp-3-161-2003>, 2003.
- 875 Schervish, M. and Donahue, N. M.: Peroxy radical kinetics and new particle formation, *Environ. Sci. Atmos.*, 1, 79-92,  
876 <https://doi.org/10.1039/d0ea00017e>, 2021.
- 877 Shen, H., Vereecken, L., Kang, S., Pullinen, I., Fuchs, H., Zhao, D., and Mentel, T. F.: Unexpected significance of a minor  
878 reaction pathway in daytime formation of biogenic highly oxygenated organic compounds, *Sci. Adv.*, 8, eabp8702,  
879 <https://doi.org/10.1126/sciadv.abp8702>, 2022.
- 880 Shen, H., Zhao, D., Pullinen, I., Kang, S., Vereecken, L., Fuchs, H., Acir, I. H., Tillmann, R., Rohrer, F., Wildt, J., Kiendler-  
881 Scharr, A., Wahner, A., and Mentel, T. F.: Highly Oxygenated Organic Nitrates Formed from NO(3) Radical-Initiated  
882 Oxidation of  $\beta$ -Pinene, *Environ. Sci. Technol.*, 55, 15658-15671, <https://doi.org/10.1021/acs.est.1c03978>, 2021.
- 883 Shilling, J. E., Chen, Q., King, S. M., Rosenoern, T., Kroll, J. H., Worsnop, D. R., DeCarlo, P. F., Aiken, A. C., Sueper, D.,  
884 Jimenez, J. L., and Martin, S. T.: Loading-dependent elemental composition of  $\alpha$ -pinene SOA particles, *Atmos. Chem.*  
885 *Phys.*, 9, 771-782, <https://doi.org/10.5194/acp-9-771-2009>, 2009.
- 886 Vereecken, L. and Nozière, B.: H migration in peroxy radicals under atmospheric conditions, *Atmos. Chem. Phys.*, 20, 7429-  
887 7458, <https://doi.org/10.5194/acp-20-7429-2020>, 2020.

- 888 Vereecken, L., Müller, J.-F., and Peeters, J.: Low-volatility poly-oxygenates in the OH-initiated atmospheric oxidation of  $\alpha$ -  
889 pinene: impact of non-traditional peroxy radical chemistry, *Phys. Chem. Chem. Phys.*, 9, 5241-5248,  
890 <https://doi.org/10.1039/b708023a>, 2007.
- 891 Wildt, J., Mentel, T. F., Kiendler-Scharr, A., Hoffmann, T., Andres, S., Ehn, M., Kleist, E., Müsgen, P., Rohrer, F., Rudich,  
892 Y., Springer, M., Tillmann, R., and Wahner, A.: Suppression of new particle formation from monoterpene oxidation by  
893 NO<sub>x</sub>, *Atmos. Chem. Phys.*, 14, 2789-2804, <https://doi.org/10.5194/acp-14-2789-2014>, 2014.
- 894 Xu, L., Møller, K. H., Crouse, J. D., Otkjær, R. V., Kjaergaard, H. G., and Wennberg, P. O.: Unimolecular reactions of  
895 peroxy radicals formed in the oxidation of  $\alpha$ -pinene and  $\beta$ -pinene by hydroxyl radicals, *J. Phys. Chem. A*, 123, 1661-1674,  
896 <https://doi.org/10.1021/acs.jpca.8b11726>, 2019.  
897